EUROPEAN ORGANIZATION FOR NUCLEAR RESEARCH
European Laboratory for Particle Physics
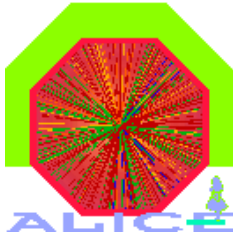
The Geometry Monitoring System of the ALICE Muon Spectrometer: Simulation results

Authors:

P. Pillot[1], J.-Y. Grossiord[1], V. Kakoyan[2], R. Tieulent[1]

[1] IPN-Lyon, IN2P3-CNRS et Université Claude Bernard, Lyon-I, France
[2] Yerevan Physics Institute, Br. Alikhanyan St. 2,375036 Yerevan, Armenia

Abstract:

Movements of the tracking chambers of the ALICE Muon Forward Spectrometer will be measured by the Geometry Monitoring System (GMS). This system is made of optical devices named BCAM and PROX. The simulations show that the GMS allows to measure the relative displacements of two chambers - which are the main source of inaccuracy - with a resolution better than 30 μm in the bending direction of tracks. It reduces the contribution of misalignment to sagitta and Y mass resolutions to about 16 μm and 6 MeV/c2 respectively. These resolutions are not much affected by optical element mispositioning, but much more sensitive to the optical resolution of BCAMs, mainly induced by thermal gradients and fluctuations. Finally, the simulations show that the GMS is robust against breakdowns.

Contents

1 Introduction

The ALICE Forward Muon Spectrometer [1, 2] has to measure the dimuon differential cross-sections with a mass resolution, $\Delta M_{\mu^+\mu^-}/M_{\mu^+\mu^-}$, of about 1% in the Υ mass region ($M_{\mu^+\mu^-} \sim 10$ GeV/c^2). It corresponds to $\Delta M_{\mu^+\mu^-} = 100$ MeV/c^2. A lack of information about the tracking chamber (TC) positions induces a loss of mass resolution. The problem is that TCs will move when the dipole magnet and the electronics are turned on. These movements are expected to be of the order of a few millimeters. It is thus necessary to use a Geometry Monitoring System (GMS) for their control [3, 4]. This system can be divided in three parts, each of which measures one of the three kinds of movements. First, the Longitudinal Monitoring System (LMS) monitors the relative displacements of the chambers. Second, the External Monitoring System (EMS) monitors the global displacement of the spectrometer. Third, the Transverse Monitoring System (TMS) monitors the deformations of the chambers.

After reviewing the required performances of the spectrometer (Section 2), we present the optical devices which will be used (Section 3) and their implementations into the GMS (Section 4). We describe simulation method (Section 5) and results showing the efficiency of the LMS (Section 6) in the case where chambers are rigid modules. Different choices for the EMS setup and their respective performances are also presented (Section 7). Next, we study the dependence of the LMS efficiency on several parameters such as mounting precisions and resolutions of the optical systems (Section 8). Chambers from stations 3 to 5 are made of two separated half planes. As these ones are not rigidly fixed together, individual half plane displacement may occur. We evaluate (Section 9) the efficiency of the LMS to measure such displacements and we present the setup used to improve these measurements. While the chamber (or half chamber) deformations are not expected to directly affect a lot the mass resolution, we show (Section 10) that they largely affect it indirectly through the deterioration of LMS efficiency. The Transverse Monitoring System (TMS) solving this problem is also presented in this Section. Finally, the sturdiness of the GMS regarding breakdowns of optical devices is studied (Section 11).

2 Requirements for monitoring

The mass resolution is expected to be better than 1%, corresponding to 100 MeV/c^2 around the Υ family masses. The broadening of the mass spectrum is mainly due to the front absorber and to the TCs [5]. The front absorber contribution comes from the multiple scattering ($\sigma_M \simeq 45$ MeV/c^2), and the energy loss fluctuation ($\sigma_M \simeq 48$ MeV/c^2) with a mass spectrum deformation. The TCs contribution comes from intrinsic resolutions and from multiple scattering ($\sigma_M \simeq 60$ MeV/c^2). All these quantities are given by AliRoot [6] for the Υ, and induce a total mass resolution of 90 MeV/c^2. As a result, and in order to stay below the required 100 MeV/c^2, the contribution to the mass resolution due to the bad alignment of TCs should not exceed 44 MeV/c^2.

The effect of bad alignment on the mass resolution depends on the momentum of muons. In order to study the quality of the alignment independently on any physical quantity, we will also look at the sagitta resolution. We thus have to translate the re-

quirement on the mass resolution into a requirement on the sagitta resolution. In the small angle approximation, the dimuon mass can be calculated using muon momenta (p) and the dimuon opening angle ($\theta_{\mu\mu}$) by:

$$M \simeq \sqrt{p_1 p_2 \theta_{\mu\mu}{}^2} \tag{1}$$

One can deduce the relative mass resolution as follows:

$$\frac{\sigma_M}{M} = \sqrt{\left[\frac{\sigma_{p_1}}{2p_1}\right]^2 + \left[\frac{\sigma_{p_2}}{2p_2}\right]^2 + \frac{cov(p_1, p_2)}{2p_1 p_2} + \left[\frac{\sqrt{p_1 p_2}}{M}\sigma_{\theta_{\mu\mu}}\right]^2} \tag{2}$$

where the term $\frac{cov(p_1,p_2)}{2p_1p_2}$ takes into account the correlation between momenta of the two muons.

The bad TCs alignment will affect the mass resolution by three different ways. First, a relative chamber mispositioning will change the bend of tracks which is directly correlated to the muon momentum (using the magnetic field), namely the sagitta of muons. The relative mispositioning will make the mass resolution worse principally through the term $\frac{\sigma_p}{p}$. Second, a global spectrometer mispositioning will rather change position and orientation of tracks. It will make the mass resolution worse principally through the term $\sigma_{\theta_{\mu\mu}}$. Nevertheless, this effect is expected to be low because the two muons will be affected in the same way. Third, a chamber deformation will move the point of impact of the muons and affect the momentum measurements. Nevertheless, since these movements occur in the beam axis direction, this effect is expected to be low. As a result, the mass resolution is expected to be much more sensitive to the chamber relative alignment efficiency. The equation (2) can then be rewritten as follows:

$$\frac{\sigma_M}{M} \simeq \sqrt{\left[\frac{\sigma_{s_1}}{2s_1}\right]^2 + \left[\frac{\sigma_{s_2}}{2s_2}\right]^2 + \frac{cov(s_1, s_2)}{2s_1 s_2}} \tag{3}$$

where we used the fact that the sagitta of a track is inversely proportional to the muon momentum.

The two muons have opposite curvatures in the magnetic field. The fake sagitta induced by chamber mispositioning will increase the momentum of one muon and decrease the momentum of the other. These two opposite effects will compensate one another in the mass calculation. In fact, it was shown by simulation that if the errors in the momentum determination are due to alignment problems, we have:

$$\sigma_{s_1}^2 \simeq \sigma_{s_2}^2 \simeq -cov(s_1, s_2) \tag{4}$$

Therefore, we can see that there are two extreme cases for the estimation of the GMS contribution to the mass spectrum, namely:

- muons with momenta of the same order of magnitude,

- muons with momenta largely different.

4

In the first case we have:

$$p_1 \simeq p_2 \Leftrightarrow s_1 \simeq s_2 \Rightarrow \frac{\sigma_M}{M} \simeq 0 \tag{5}$$

and in the case where one muon has a high momentum and the second one a small momentum:

$$p_1 \gg p_2 \Leftrightarrow s_1 \ll s_2 \Rightarrow \frac{\sigma_M}{M} \simeq \frac{\sigma_{s_1}}{2s_1} \tag{6}$$

We are now able to calculate the requirement on the sagitta resolution. In order to be over constrained, we use the worse case where two muons have very different momenta ($p_1 \gg p_2$). Moreover, as the mass resolution depends on the momentum of muons, it is safe to define the requirement on the sagitta resolution using high momentum muons. Thus, we are sure that the mass of any Υ will be reconstructed with sufficient accuracy when the sagitta resolution is below requirement. Using muons of 100 GeV/c (at the absorber end) which have a sagitta between 7 and 8 mm, we find that the contribution of the alignment to the sagitta resolution should not exceed 70 μm.

The aligment is done in two steps. First, a calibration run measures the initial position of the chambers, using straight tracks of muons (with the dipole magnet switched off). Then, during the physics runs, the GMS periodically measures the chamber displacements and deformations. The achieved accuracies of the calibration run were calculated by simulation [7] and the following values were found: $\sigma_{\theta_{\mu\mu}} \simeq 0.1$ mrad and $\sigma_{sagitta} \simeq 20$ μm. Taking into account these results, geometrical requirement for the GMS is about 68 μm on sagitta resolution.

3 Optical devices
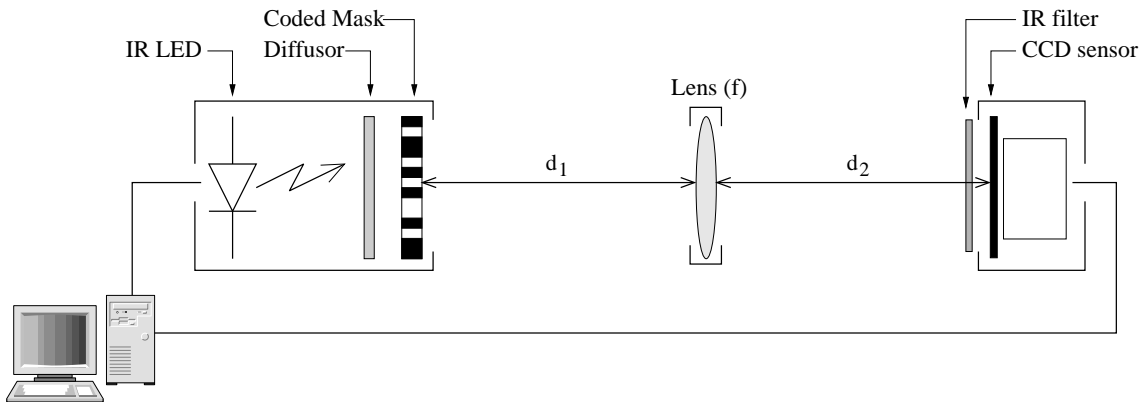
3.1 Introduction

Figure 1: Layout of a RASNIK system.

The two selected optical devices are derived from the RASNIK system [10] which was developed by NIKHEF, used for the L3 experiment and adopted for endcaps and barrel monitoring in the ATLAS detector [8]. Its principle is simple (Fig. 1): a CCD camera films a draughtboard (Fig. 2) through a lens. Thanks to coded lines printed across its surface at regular distance in both directions, not the entire mask but just an entire coded cell has to be filmed in order to know unambiguously where the CCD is looking at. In its normal configuration, the three RASNIK elements are mounted separately. A displacement of the image of the mask on the CCD is due to a relative displacement of the three supports. In order to get a good resolution with this system, it is very important to respect the configuration imposed by the relation between the focal length of the lens and the relative distances between each element which is given by the following equation:

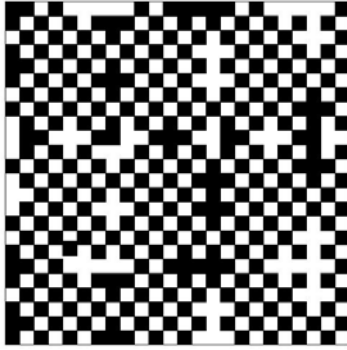$$\frac{1}{d_{lens-CCD}} + \frac{1}{d_{lens-mask}} = \frac{1}{f} \tag{7}$$

Figure 2: A coded mask.

Because we need to film at least one entire coded cell, the magnification must not be too big. On the other hand, if the magnification is too low, a large part of the mask will be filmed and, due to the CCD resolution, the central part of the filmed zone will not be measured accurately. As a consequence, the magnification must be of the order of one to have a properly working RASNIK device. Distances between the two first and the two last stations of the spectrometer are very different as compared to distances between the three inner stations. It is then impossible to use RASNIKs to monitor the stations 1, 2 and 3, and the stations 3, 4 and 5. Moreover, it was shown that the RASNIK system alone cannot provide enough constraint to unambiguously monitor five TCs, whatever the number of lines [9]. This can be extended to the entire spectrometer. For all these reasons, the RASNIK system, as described above, will not be used to monitor the relative positions of the TCs. The two derivative systems presented below are much well adapted and their installation is easier.
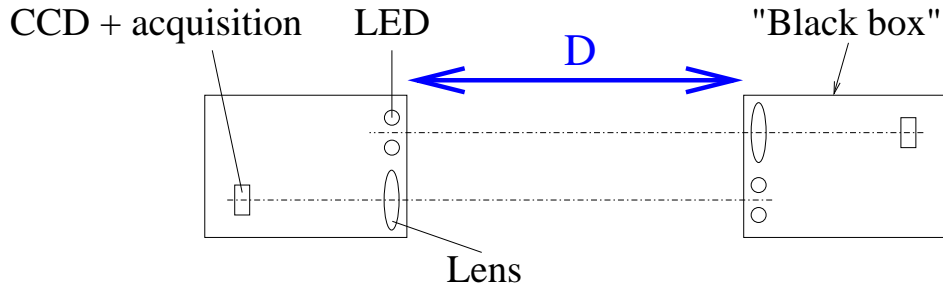
Figure 3: Layout of a BCAM line.

3.2 The BCAM device

Description: the BCAM [11] is a long range system (Fig. 3) with CCD and lens mounted on the same support. It is used as soon as distances to be monitored are larger than about 1 m (between stations, between spectrometer and external points on the walls and between the four corners of each (half) chamber). It is impossible to read a mask in such a configuration. It is thus replaced by two LEDs. In order to improve installation precisions, LEDs are mounted on the CCD and lens box. A BCAM line (two boxes looking at each other) is thus made of two optical lines. This is also very useful to have an efficient symmetric system.

Measurements: measuring the centroid of the LEDs images allows to find their positions on the CCD with a high resolution. Thus, each BCAM line provides eight measurements which are x and y positions of the four LEDs. We have an indication of the distance between the two boxes by measuring the distance between the two LED images, but only the transverse positions of LEDs can be determined with a good accuracy. The principle of calculation of BCAM measurements is given in Annexe A.

Resolutions: the CCD resolution was measured at Brandeis University (which will provide us with BCAM and PROX systems). They obtained an intrinsic resolution of 0.1 μm. This value corresponds to a 1.3 μrad angle resolution with a 7.5 cm long box. If we include effects of normal air fluctuations for a 8 m BCAM range (measured during these tests) and effects of mounting uncertainties of each element in boxes, we obtain a resolution on the CCD measurement of about 0.5 μm in both directions. As the BCAM films point sources, the image does not need to be focused (the centers of intensity distributions do not change when defocusing). This makes easy the installation of the BCAM boxes.

3.3 The PROX device

Description: the PROX is a short range RASNIK (Fig. 1) with CCD and lens mounted on the same support. It is used for distances of the order of 30 cm (between chambers of each station). Contrary to the BCAM, each PROX element needs to be set at their optimal interdistance (respecting Eq. (7)) with a tolerance of a few millimeters, so that a good resolution can be achieved.

7

Measurements: by decoding the image recorded by the CCD, we can find:
- the part of the mask which is filmed (position x and y on the mask),
- the magnification M of this filmed part,
- the rotation angle α around the optical axis of the mask relative to the CCD (with a low resolution).

The principle of calculation of PROX measurements is given in Annexe B.

Resolutions: the PROX resolution is different from the BCAM one due to the different image analysis methods. Same kind of tests carried out with the BCAM were done with the RASNIK [10]. These results can be applied to PROX and are as follows: $\sigma_x = 1\ \mu$m, $\sigma_y = 1\ \mu$m, $\sigma_M = 5 \cdot 10^{-5}$ and $\sigma_\alpha = 0.2$ mrad. It can be recalled that, in order to achieve these resolutions, it is very important to respect the configuration imposed by the lens focal length to the relative distances between each element (Eq. (7)).

4 Setup and procedure to monitor the chambers

The goal of the Geometry Monitoring System is to measure the displacements of the chambers starting from their initial positions (measured by the calibration runs), and the chamber deformations. The system is made of several PROX and BCAM lines installed through the spectrometer. The setup finally adopted is presented in Fig. 4. The number and location of BCAM and PROX lines were defined by simulation, in order to properly constrain all deformation and displacement parameters. The different steps of these simulations are presented in the next Sections.

The procedure used to perform the monitoring is as follows:

1. Before installing the chambers inside the cavern, the position of all optical elements will be measured relative to the chamber's planes (TCs 1-4) and the slats supports (TCs 5-10), by the CERN survey group.

2. During the calibration run, images from all optical lines will be recorded. These images, being correlated with the initial geometry of the spectrometer, will be kept as references.

3. After switching on the magnet, images from all optical lines will be periodically recorded during the physics data taking and compared to the references. Image displacements will be extracted.

4. Chamber displacements and deformations will be adjusted from all measurements, using the MINUIT fitter. This step is described in detail in Section 5.1.

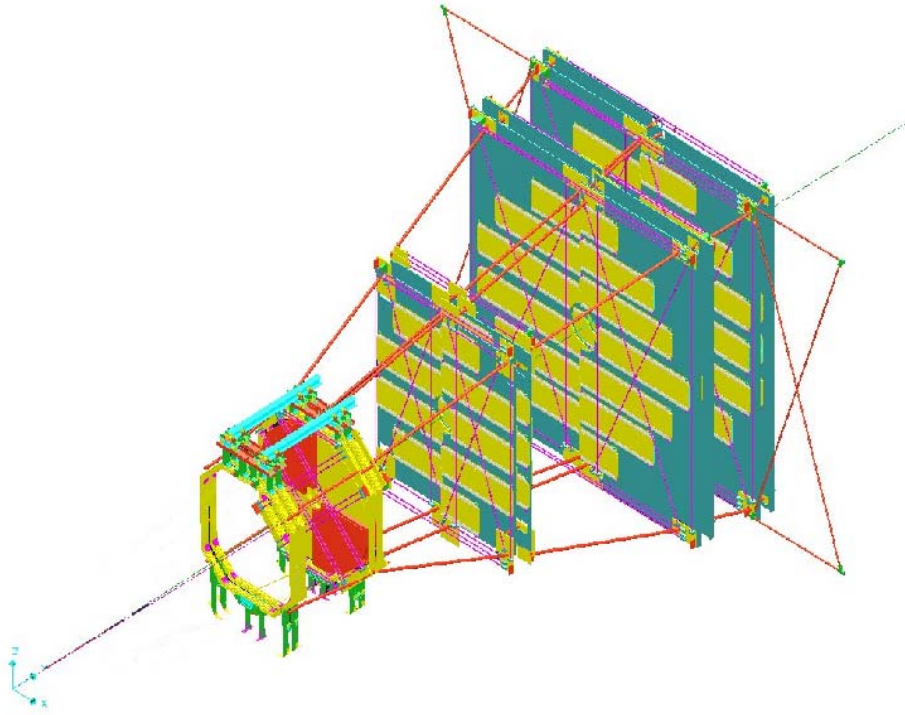A schematic view of the procedure is shown in Fig. 5.

Figure 4: Layout of the GMS setup. Lines between chambers of each station are PROXs. All other lines are BCAMs.
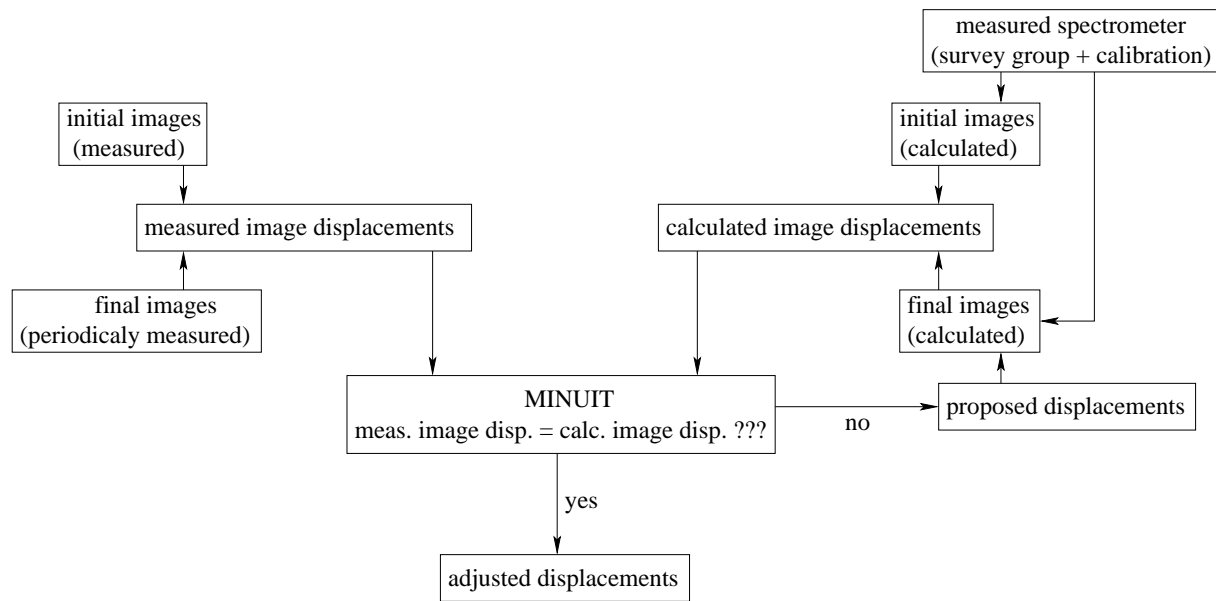
Figure 5: Procedure used to perform the monitoring.

5   Simulation method

The goal of these simulations is to find the best way to perform the GMS, then to evaluate its performances which depend on several parameters:

- the number and position of external links,

- the wall deformations,

- the efficiency of the calibration run,

- the accuracy on the measurement of optical element positions,

- the resolution of optical systems.

5.1   Simulation procedure

Simulations are performed as presented below. A schematic view of the procedure is also shown in Fig. 6. The difference between this procedure and the one presented in the previous section (Fig. 5) is that the measured spectrometer configuration and the optical measurements are obtained by simulation.

Figure 6: Simulation procedure used to evaluate the monitoring efficiency.

The procedure used to perform the simulations is as follows:

1. Simulation of optical measurements (left part in Fig. 6).

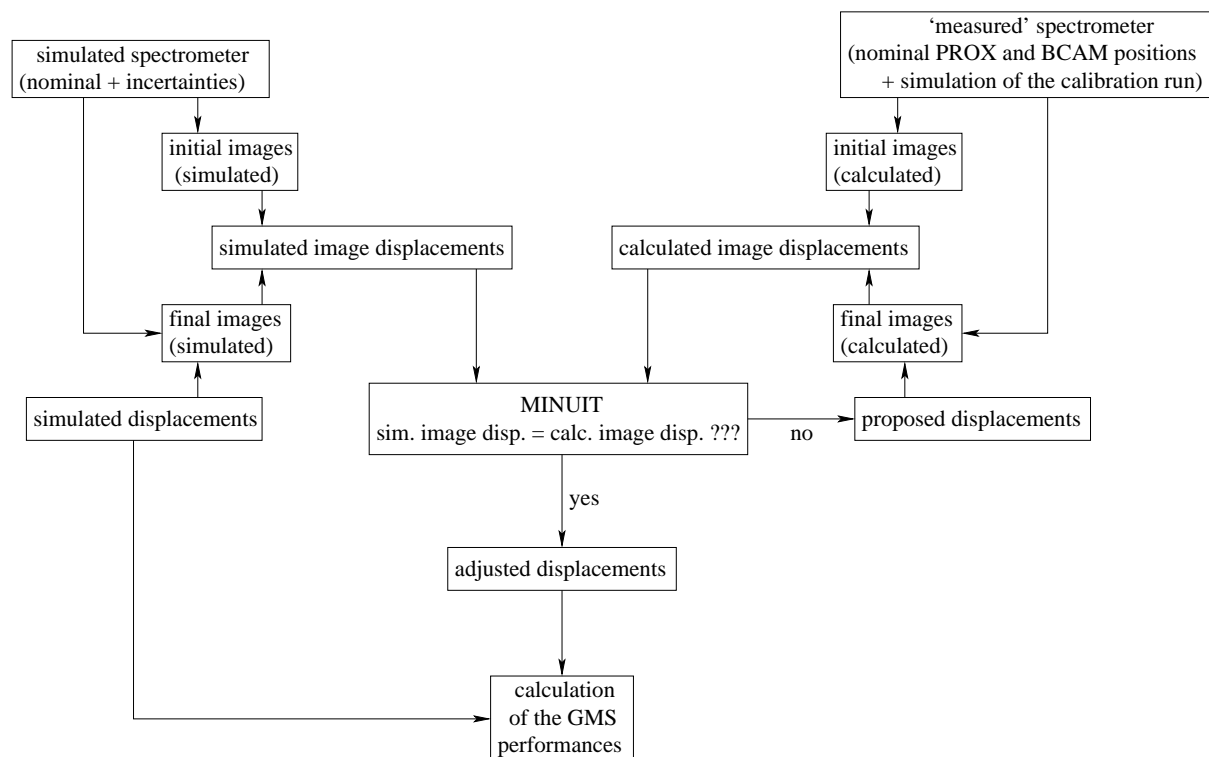   (a) Simulation of a 'real' spectrometer configuration (chamber and optical element positions) around the nominal one using the installation accuracies of chambers and optical elements.

   (b) Random displacements and deformations of all chambers.

   (c) Calculation of all optical line measurements (image modifications induced by these movements, taking into account intrinsic resolutions).

2. Use of MINUIT to extract chamber deformations and displacements. Only the following known quantities must be used:

   - simulated optical measurements (left in Fig. 6),

   - nominal positions of optical lines (top right in Fig. 6),

   - initial positions of chambers obtained by simulation of the calibration run applied on the 'real' spectrometer configuration (top right in Fig. 6).

   MINUIT [12] is based on a χ^2 minimisation by adjusting several free parameters (here chamber deformations or displacements). χ^2 is defined as follows:

   $$\chi^2 = \sum_i \frac{(dep_{sim_i} - dep_{calc_i})^2}{\sigma^2_{sim_i}}$$

   where:

   - dep_{sim_i} is the ith optical measurement simulated in the first step of the procedure.

   - dep_{calc_i} is the ith optical calculated measurement. In this case, the chambers are moved from the 'measured' configuration of the spectrometer given by the simulated calibration run, using the displacement or deformation parameters proposed by MINUIT. For this calculation, the nominal positions of optical lines are used. It corresponds to the right part in Fig. 6.

   - $\sigma_{sim_i} = \sigma_{intrinsic\ resolution} \oplus \sigma_{installation}$ represents the confidence level of the ith simulated optical measurement.

   In fact, MINUIT adjusts the chamber deformation or displacement parameters in order to retrieve as well as possible the simulated optical measurements, taking into account the confidence level given for each one.

3. Comparison between displacements and deformations randomly introduced in the first step and the ones adjusted by MINUIT. Study of effects of mispositioning on several relevant parameters.

These successive steps are repeated many times in order to build distributions of residuals (between 'real' and reconstructed values) of all the quantities used to evaluate the monitoring efficiency. All the resolutions given later in this note will be extracted from these distributions with an accuracy between 5% and 10% due to statistics.

11

5.2   Analysing programs

Two programs are used to compare results from monitoring with the quantities really introduced in the simulation. The first program calculates the reconstruction accuracies of chamber deformations and displacements. It also calculates the fake sagitta introduced by wrong displacements on straight tracks passing through the spectrometer. The second program is AliRoot [6] modified in order to move the track hits with their chambers before the reconstruction procedure. This modification allows to account for residuals between 'real' and reconstructed chamber displacements, namely to simulate chamber displacements badly corrected by the monitoring system. AliRoot allows to evaluate monitoring performances regarding physical quantities such as muon momentum, dimuon opening angle, Υ mass, Υ transverse momentum and Υ rapidity. 2000 Υ were generated and forced to decay into two muons. The momentum distribution of these muons at the absorber end is presented in Fig. 7.
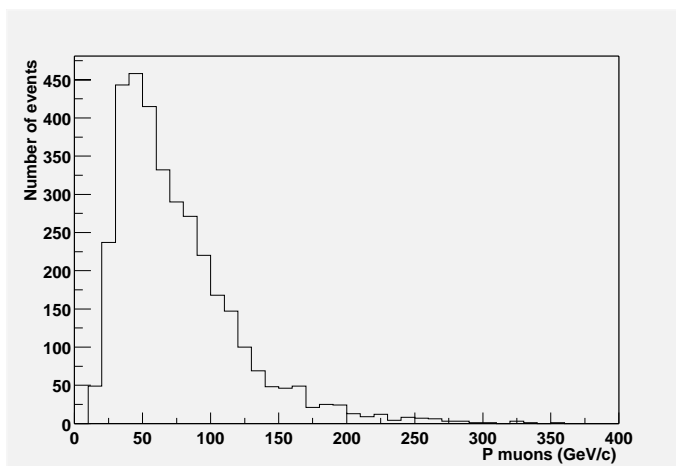

Figure 7: Muon momentum distribution at the end of the front absorber.

Requirements on sagitta resolution (Section 2) were calculated using 100 GeV/c muons. Nevertheless, we can see on the previous distribution (Fig. 7) that most of the muons used to calculate the Υ mass resolution have a momentum below 100 GeV/c (the mean value is around 70 GeV/c). Such muons have a better relative accuracy on momentum than 100 GeV/c muons with the same chamber mispositioning, which induces a better mass resolution. Consequently, results from AliRoot will be about 1.5 to 2 times better than the expected ones looking at results from the other program (when we use the correspondence between 44 MeV/c and 70 μm coming from requirement). This factor is a security factor on the mass resolution. Another remark is that the program which calculates resolutions on geometrical quantities uses analytical methods and not a fitting procedure like AliRoot does. As a result, resolutions coming from this program are about 10% worse than they should be. Despite of the differences coming from the use of two different programs, results from both are useful to correctly evaluate the GMS performances. The sagitta allows to evaluate the performances in the worse cases and independently on the characteristics of particles. The mass gives access to the mean performances of the GMS.
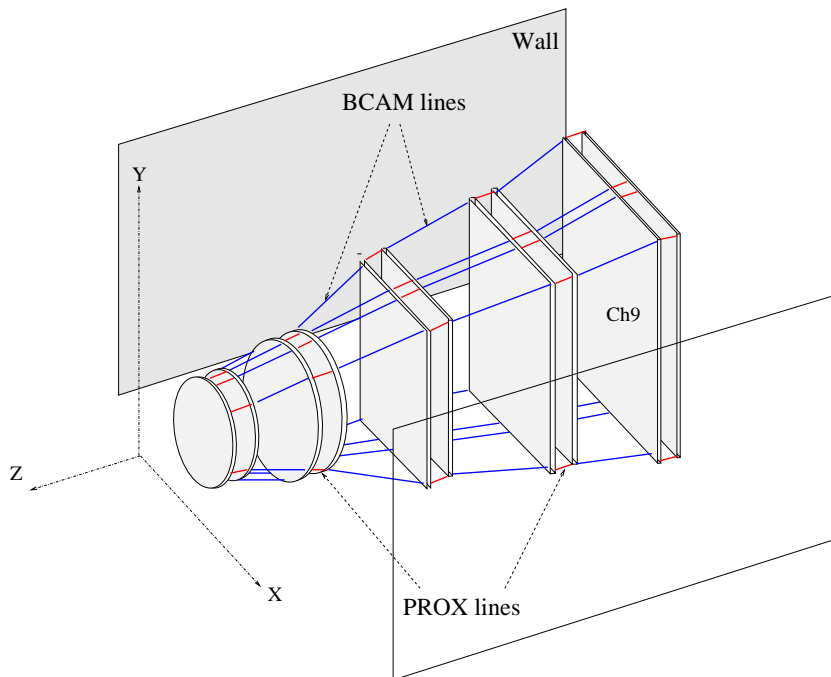
Figure 8: Layout of the LMS setup. Devices between stations are BCAMs, between chambers in each station PROXs.

6 Monitoring of 10 rigid chambers: the LMS

The goal of the GMS is to measure the chamber displacements which are the main source of mass resolution loss. This is done with the Longitudinal Monitoring System (LMS) presented in Fig. 8. However, since BCAM and PROX are only sensitive to the relative movements of their elements, the LMS is only able to measure the relative displacements of the chambers. It means that one of these latter must be monitored by another system in order to be used as an absolute reference for the LMS. The other chambers will then be monitored by the LMS relative to this one. This other system is the EMS, presented in the next Section. Only TC9 can be easily monitored by the EMS. It was chosen as the reference chamber for the LMS. The external monitoring of the TC9 is supposed to be perfect in this Section. Its 6 displacement parameters are fixed. All chambers are also supposed to be rigid modules. The mounting accuracies of each optical element were fixed to 0.5 mm in position and 0.5 mrad in orientation in the simulations. Optical resolutions of both BCAM and PROX systems were fixed to their nominal values (Section 3).

Several quantities can be extracted to evaluate the LMS efficiency:

- the reconstruction accuracies of the chamber relative displacements (Table 1),

- the sagitta resolution, directly correlated to the previous quantities,

- the Υ mass resolution which depends on momentum and opening angle resolutions of the two muons.

$\sigma_{i,j}$	Tracking chamber pair (i,j = 1-10)								
(μm)	1,2	2,3	3,4	4,5	5,6	6,7	7,8	8,9	9,10
σ_x	5	11	4	18	3	14	4	7	3
σ_y	6	12	4	19	4	16	4	7	4
σ_z	2	24	2	30	3	12	5	19	6

Table 1: Measurement resolution of the chamber relative displacement, in the three directions (x: horizontal, y: vertical, and z: along the beam).
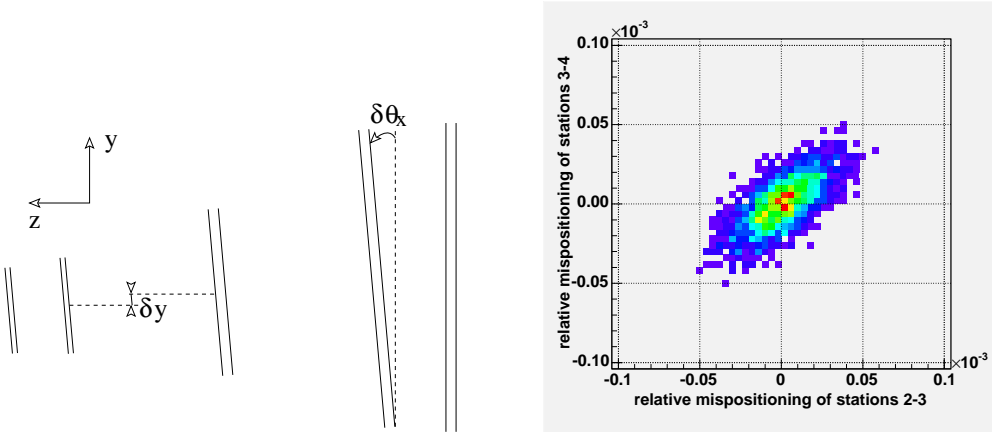

Figure 9: Example of propagation of errors (left); correlation between relative mispositioning of stations 2 and 3, and of stations 3 and 4 (right).

As we can see from Table 1, the LMS allows to measure the relative displacements of TCs with a precision better than 20 μm in the y direction. Moreover, due to the fact that chambers are monitored relatively to their nearest neighbourgs, a bad displacement measurement of a chamber is propagated to the others down to the first one. For instance, a bad rotation measurement $\delta\theta_x$ of TC8 will induce an error δy on the relative displacement measurement between TC4 and TC5 in the y direction, as illustrated in Fig. 9 (left). Such a propagation of errors results in relative displacement measurement uncertainties of each couple of chambers positively correlated the ones to the others, as we can see in Fig. 9 (right). Since the sagitta measurement is less affected by the propagation of errors (only the positions of stations 2 and 4 relatively to station 3 are meaningful), the sagitta resolution is better than the expected one looking at individual results on relative displacement measurements: 6.7 μm is obtained (Fig. 10), which is much better than requirements.

Finally, quantitative results from AliRoot are as follows: $\sigma_{M_\Upsilon} = 2.6$ MeV (Fig. 11), $\frac{\sigma_p}{2 \cdot p} = 3.2 \cdot 10^{-4}$ and $\frac{\sqrt{p_1 \cdot p_2}}{M_\Upsilon} \cdot \sigma_{\alpha_{\mu\mu}} = 10^{-5}$.

As expected, the relative mispositioning of chambers affects principally the momentum resolution (correlated to the sagitta), and not the opening angle resolution. Effectively, the same misplacement occurs for the intersection points of the two muons on each chamber. Therefore, the two tracks are affected in the same way and their angles at the end of the front absorber are reconstructed with about the same error. We can finally observe that
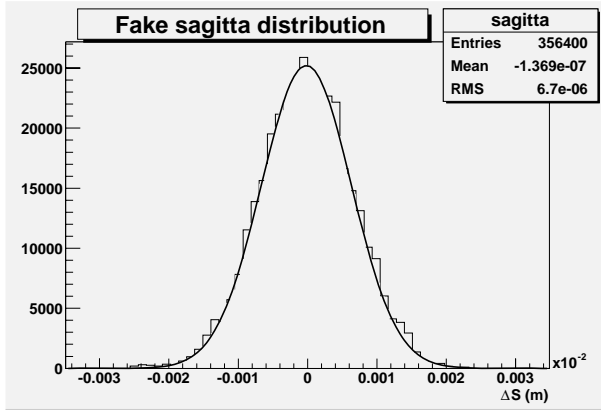
Figure 10: Distribution of fake sagitta introduced on straight tracks passing through the spectrometer. These tracks come from muons with momentum >100 GeV/c² at the absorber end.
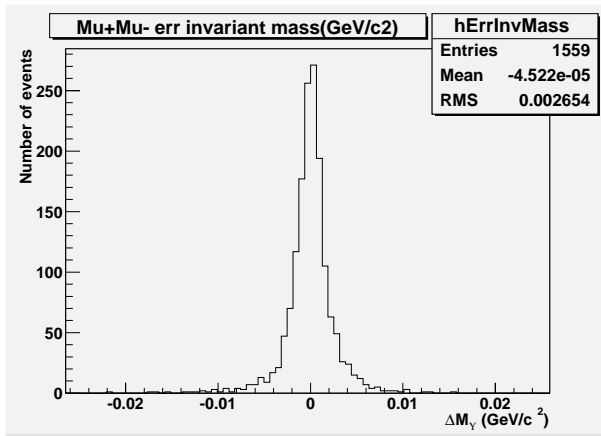
Figure 11: Mass resolution.

the mass resolution obtained with the LMS is much better than requirements.

7 Choice of the EMS setup

As already stated in the previous Section, the goal of the External Monitoring System (EMS) is to monitor the TC9 in order to provide the LMS with a reference chamber and to provide us with an absolute monitoring of the entire spectrometer. The ideal monitoring of TC9 should be performed through fixed reference. Unfortunately, as such a reference does not exist, we will choose the ALICE cavern walls which are expected to move very slowly during the run time. Nevertheless, it is possible to correctly control the vertical displacement (in the bending direction of tracks) of a point on the wall using the Hydrostatic Leveling System [13] (HLS) of ALICE. This system is able to provide this displacement with an accuracy better than 10 μm. The goal of this Section is to find the best setup to link TC9 to the walls, using BCAMs alone or coupled to the HLS. One took rms values of 1 mm and 1 mrad for the wall deformations to simulate effects during a

long period (physical runs will go on several months without any calibration), and 10 μm in the bending (vertical) direction when the HLS is used. In this case, hydrostatic vessels must be put 50 cm under the beam axis, on the hydrostatic line. All the chambers were still supposed to be rigid modules. The other parameters (optical element positioning accuracies and optical system resolution) were fixed to the same values as in the previous Section.

Displacement parameters of all chambers are largely correlated to displacement parameters of TC9 (measurements of optical systems are relative). Moreover, the confidence level (σ_{mes_i}) of internal and external optical measurements are not of the same order of magnitude (because of errors induced by the wall deformations). Consequently, if one wants MINUIT to converge accurately, the monitoring procedure must be divided into two successive steps: first, the external monitoring to find the TC9 displacements using the external links, and second, the longitudinal monitoring to find all other chamber displacements knowing the TC9 ones.

In order to evaluate the performances of the EMS, several quantities can be extracted:

- reconstruction accuracies of TC9 displacements (3 translation and 3 rotation parameters),

- effect on the Υ mass resolution which can appear through momentum and opening angle resolutions of the two muons,

- effect on the Υ transverse momentum and rapidity resolutions.

Results obtained with different setups are given in Table 2. The setup 0 is the reference. The external monitoring is perfect. Results are given by the LMS and are the same as in the previous Section. The setup 1 (Fig. 12) efficiently performs the external monitoring without vessels. The setup 2 (Fig. 13) requires only two vessels, but we can see (Table 2) that it is not efficient at all, because it provides a very bad control of the rotation around the x axis. The setup 3 (Fig. 14) requires four vessels, it is the most efficient one. The setup 3' is identical to the setup 3, without using HLS.

	σ_x	σ_y	σ_z	σ_{θ_x}	σ_{θ_y}	σ_{θ_z}	$\frac{\sigma_p}{2 \cdot p}$	$f \cdot \sigma_{\alpha_{\mu\mu}}$	σ_{M_Υ}	$\sigma_{p_{T_\Upsilon}}$	σ_{y_Υ}
	(μm)	(μm)	(μm)	(μrad)	(μrad)	(μrad)	($\times 10^{-4}$)	($\times 10^{-4}$)	(MeV/c^2)	(MeV/c)	($\times 10^{-4}$)
0	0	0	0	0	0	0	3.2	0.1	2.6	6.4	1.6
1	808	545	500	161	47	45	3.6	1.6	3.2	47	20
2	686	53	797	727	66	3.9	4.2	4.6	6.5	168	69
3	593	53	532	10	43	3.0	3.4	1.3	2.9	17	7.0
3'	856	736	580	141	48	46	3.6	1.6	3.1	29	12

Table 2: Effects of external links on several quantities: reconstruction accuracies of TC9 displacements; relative momentum, opening angle ($f = \frac{\sqrt{p_1 \cdot p_2}}{M_\Upsilon}$), Υ mass, transverse momentum and rapidity, using AliRoot.

Displacements of all chambers are measured relative to the TC9. A bad displacement measurement of this one affects all TCs in the same way. It means that the entire spectrometer is badly replaced, but the relative position accuracies of TCs are not affected.
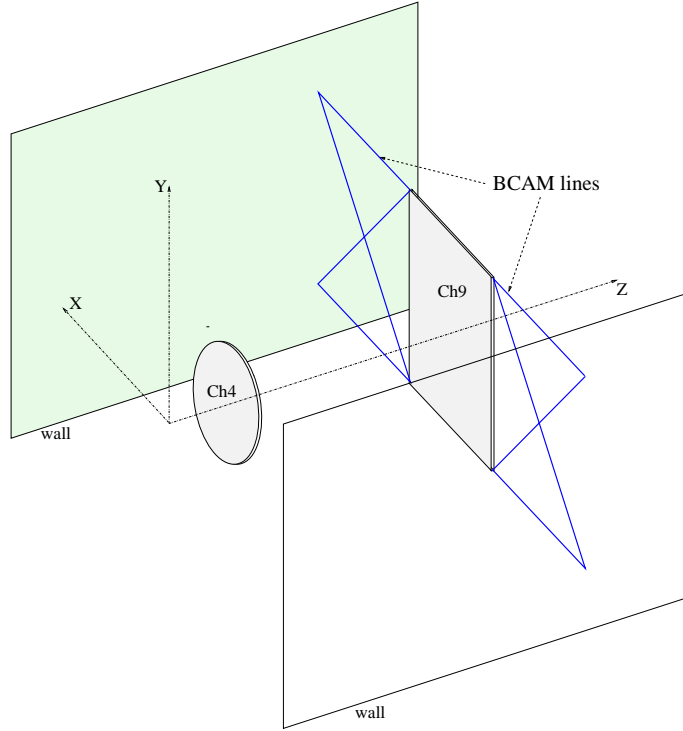
16

Figure 12: Layout of setup 1.

This is what we can observe looking at results from Table 2. Only variables depending on the global position of the spectrometer ($p_{T\Upsilon}$ and y_Υ) are really affected whereas resolution on σ_p (depending almost only on TC relative positions) is almost not. The opening angle between the two muons at the absorber end is not affected a lot by the global misplacements of the spectrometer because it depends only on the relative position of the reconstructed tracks. Nevertheless, the opening angle reconstructed at the vertex ($\alpha_{\mu\mu}$) is calculated using the Badier-Brandson method [5] which uses both the angle and the position of the muons at the absorber end. Because the position of the two muons at the absorber end is affected by a global misplacement of the spectrometer (particulary in the beam axis direction), the opening angle at the vertex is affected too (column 9 of Table 2).

The setup 2 excepted, the choice of the EMS setup does not affect largely the mass resolution. Resolutions on $p_{T\Upsilon}$ and y_Υ coming from the front absorber and the TCs themselves are 160 MeV/c and 77×10^{-4} respectively. Even the setup 1 does not change much these quantities. Consequently, all setups (the setup 2 excepted) are efficient to perform the external monitoring. Using HLS needs to add a second hydrostatic line to ALICE (only one is necessary otherwise), and vessels. The setup 1 is obviously easier to install than the setup 3. Moreover, the setup 1 is made of shorter BCAM lines than the setup 3', all within a plane common to the plane of the chamber 9. The setup 1 will be thus less affected by possible air disturbances in the cavern and also the simplest system to be installed. In conclusion, the setup 1 seems to be the most interesting to perform the external monitoring.
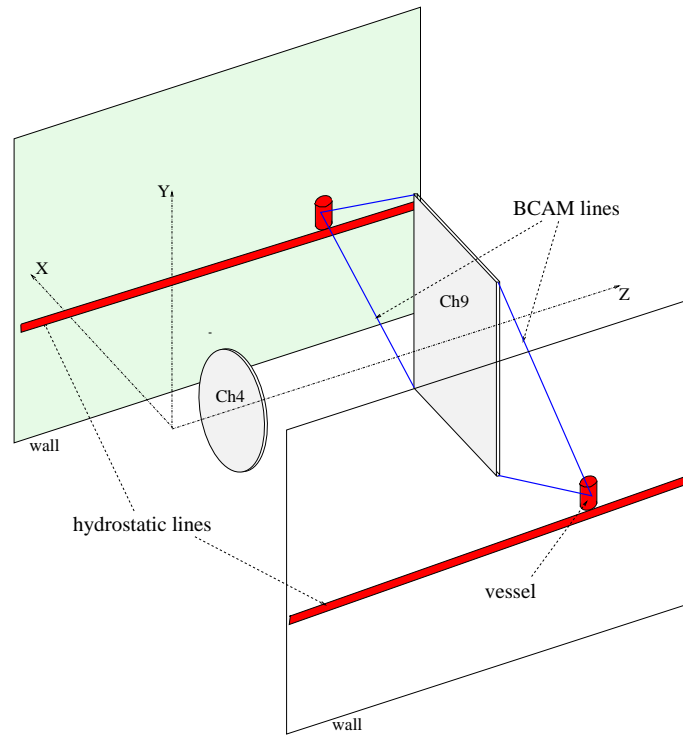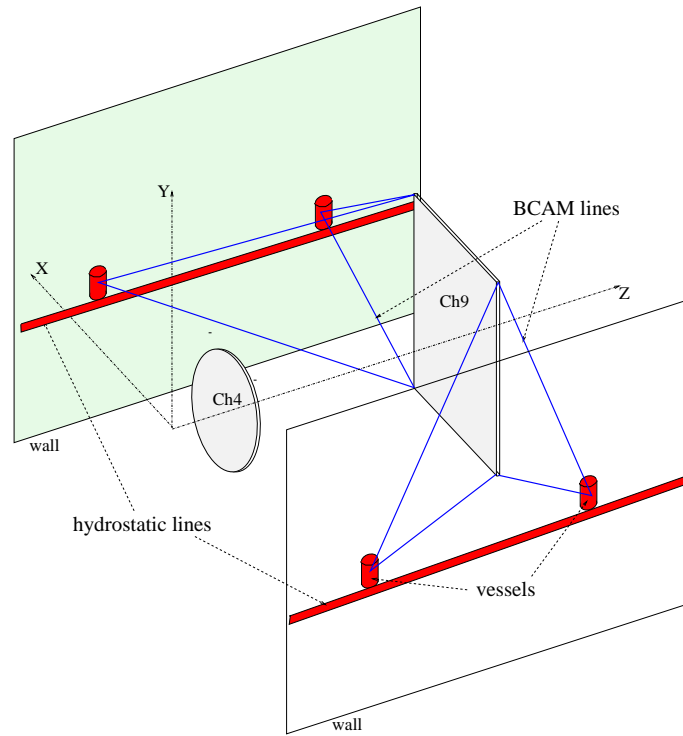
Figure 13: Layout of setup 2.

Figure 14: Layout of setup 3.

8   Effects of external parameters on the LMS

As shown in the previous Section, the Υ mass resolution does not depend a lot on the external monitoring efficiency. Moreover, this efficiency is principally lowered by the wall deformations. The other external parameters have, in comparison, almost no effect. Consequently, effects of the external parameters will be studied looking at the efficiency of the LMS only (which is less CPU time consuming). This choice is fully justified *a posteriori* in Section 11.3 where the efficiency of the GMS is simulated in its globality. All the chambers are still supposed to be rigid modules in this section.

8.1   Effects of the calibration run

The first step of the procedure used to monitor the chambers is the measurement of their initial position during a calibration run (see Section 4). The chamber displacements are then reconstructed starting from this position. Consequently, if this initial measurement is not accurate enough, the chamber displacements may be incorrectly reconstructed. In order to evaluate this effect, the performances of the LMS previously obtained (which took into account the calibration uncertainties) are compared to the ones obtained by assuming a perfect calibration. This last point is done by giving to the chambers the same initial positions to simulate their displacements and to reconstruct them. The mounting accuracy of each optical element was fixed to 0.5 mm in position and 0.5 mrad in orientation. The optical resolutions of both BCAM and PROX systems were fixed to their nominal values (Section 3).

calibration run	$\sigma_{x_{TS2-3}}$ (μm)	$\sigma_{y_{TS2-3}}$ (μm)	$\sigma_{z_{TS2-3}}$ (μm)	$\sigma_{sagitta}$ (μm)	$\frac{\sigma_p}{2 \cdot p}$ ($\times 10^{-4}$)	$f \cdot \sigma_{\alpha_{\mu\mu}}$ ($\times 10^{-5}$)	$\sigma_{M_{\Upsilon}}$ (MeV/c^2)
with	18	19	30	6.7	3.2	1.2	2.6
without	16	16	26	6.2	2.8	1.0	2.3

Table 3: Effects of the calibration run on several quantities: relative positioning accuracies of stations 2 and 3 in x, y and z directions, using straight lines uniformly distributed in the spectrometer acceptance; fake sagitta induced on these straight lines; relative momentum, opening angle ($f = \frac{\sqrt{p_1 \cdot p_2}}{M_{\Upsilon}}$) and Υ mass resolutions, using AliRoot.

As we can see in Table 3, the monitoring efficiency is almost not affected by the inaccuracy of the calibration. One can also note that several calibration procedures exist but none really affects the monitoring efficiency.

8.2   Effects of the optical element installation accuracies

A very important point of our procedure is that we measure chamber displacements and not directly chamber positions. Thus, we are not interested on the absolute position of images on CCDs but only on image displacements relative to references. As these references are also affected by the optical element mispositioning, image displacements do not suffer from these uncertainties. As a result, optical elements have not to be placed

with a very high accuracy. Nevertheless, real effects and requirements on optical element positioning accuracy were quantified by simulation. Optical resolutions of the optical devices were fixed to their nominal values (Section 3).

In a first step, we look at a few examples to understand how the optical element mispositioning affects the BCAM and PROX measurements of displacements:

BCAM: the effects of each kind of mispositioning depend, by a different way, both on the displacements and on the distance separating the two boxes, as illustrated in the following examples. The first one shows the effect of a bad longitudinal position in the case of a transverse translation of the LED. The second one shows the effect of a bad orientation around the optical axis in the case of a rotation of the CCD box around a transverse axis.

1. the LED translation (dep_{LED}) is deduced from the image displacement CCD_{mes}) with the following equation:

$$dep_{LED} = \frac{D_{LED-lens}}{d_{CCD-lens}} \cdot CCD_{mes} \tag{8}$$

from which one can calculate the effect of the longitudinal mispositioning ($\sigma_{D_{LED-lens}}$):

$$\sigma_{dep_{LED}} = \frac{dep_{LED}}{D_{LED-lens}} \cdot \sigma_{D_{LED-lens}} \tag{9}$$

2. the transverse rotation of the CCD box (rot_{CCD}) is equivalent to a translation of the LED ($rot_{CCD} \cdot D_{LED-lens}$). So the bad orientation (σ_{θ_Z}) induces a fake displacement measurement (perpendicular to the rotation axis) as follows:

$$\sigma_{dep_{LED}} = rot_{CCD} \cdot D_{LED-lens} \cdot \sigma_{\theta_Z} \tag{10}$$

As shown in the previous examples, all mispositioning effects increase when increasing the range of displacements. Taken as a whole, one observes that the measurement inaccuracy coming from a bad positioning (in all directions) decreases when increasing the distance between the two boxes, while the reverse effect occurs when the inaccuracy comes from a bad orientation (around all directions). Finally, it was observed that, on average, the BCAM measurement uncertainty, including all mispositioning effects, doesn't change when increasing the distance between the two boxes from 1 to 3 meters.

PROX: as for BCAMs, the effects of each kind of mispositioning depend on displacements by a different way, and all these effects increase when increasing the range of displacements. The PROX system is a low range system whose the distance between its two elements is fixed by the focal length. Therefore, it is not necessary to study the mispositioning dependence on this distance. One can note that when the PROX elements are displaced like they will be in the spectrometer, measurements are more sensitive to bad orientation than to bad positioning.
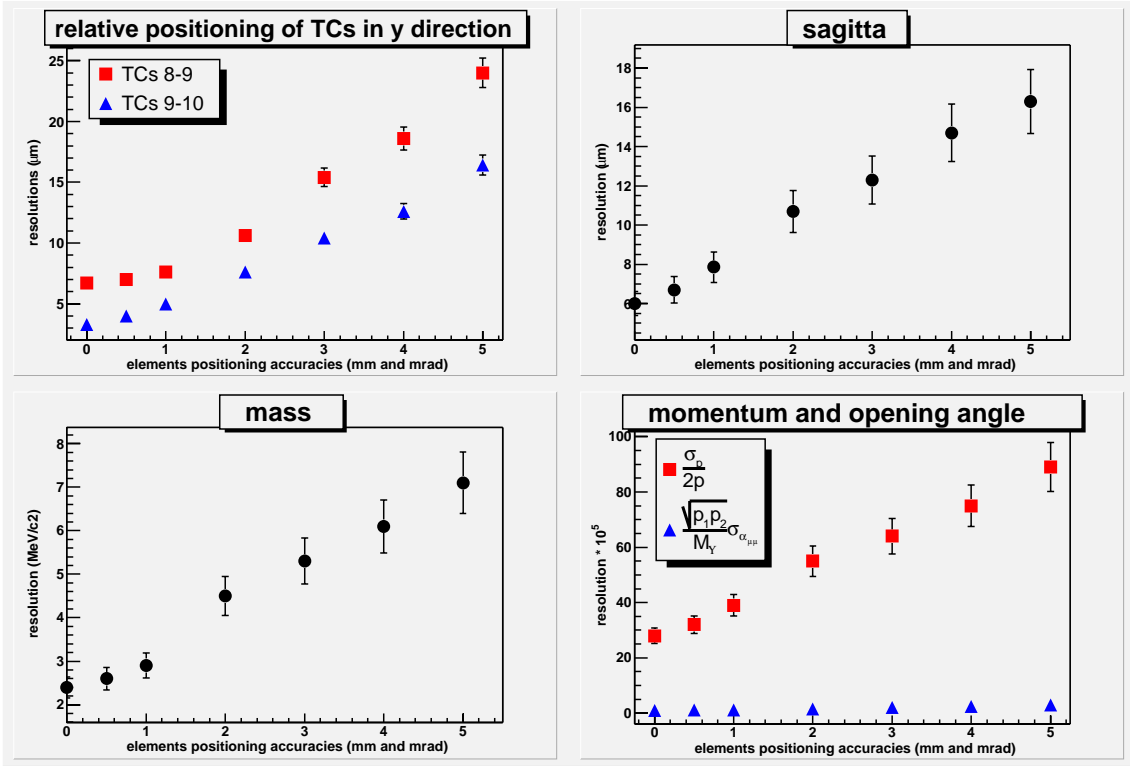
Figure 15: Effects of optical element mispositioning on several quantities: **top left:** relative positioning accuracies between TCs 8-9 (monitored by BCAMs) and 9-10 (monitored by PROXs) in bending direction, using straight tracks uniformly distributed in the spectrometer acceptance; **top right:** fake sagitta induced on these straight tracks; **bottom left:** Υ mass resolution; **bottom right:** relative momentum ($\frac{\sigma_p}{2 \cdot p}$) and opening angle ($\frac{\sqrt{p_1 \cdot p_2}}{M_\Upsilon} \cdot \sigma_{\alpha_{\mu\mu}}$), using AliRoot.

In a second step, we evaluate effects of optical element mispositioning on the monitoring efficiency. Results are summarized in Fig. 15. The values given in abscissa are the uncertainties on both position (x,y,z) and orientation ($\theta_x, \theta_y, \theta_z$) of the optical elements. The optical element mispositioning affects BCAMs and PROXs responses in a similar way, as we can see in the first figure (TCs 8-9 are monitored by BCAMs and TCs 9-10 by PROXs). Nevertheless, the intrinsic resolution is the main reason for BCAMs inaccuracy for quite small mispositioning, as shown by the horizontal start of the curve for TCs 8-9. This is due to the small magnification of these systems in their working position. Effectively, a 0.5 μm CCD resolution induces a $\simeq 9$ μm resolution on the transverse relative displacements of the elements, for an 1 meter long system. On the contrary, the intrinsic resolution given for PROXs (1 μm) is directly the resolution on the transverse relative displacements. As a consequence, mispositioning becomes the main reason of PROXs inaccuracy. The global effect of position and orientation uncertainties on the sagitta and the mass was also calculated: with a 5 mm position resolution only, one finds $\sigma_S = 12$ μm and $\sigma_M = 5$ MeV/c^2, and with a 5 mrad orientation resolution only, one finds $\sigma_S = 15$ μm and $\sigma_M = 6$ MeV/c^2. It appears that, taken in the whole, it is a little more important

21

to properly control the optical element orientation than their position. Finally, we can see from all these figures that resolutions of all geometrical and physical quantities are not much affected by the optical element mispositioning. Even with a 2 mm and 2 mrad inaccuracies in all directions, the fake sagitta is only about 10 μm and the mass resolution is not more than 4 MeV/c^2.

In situ, the installation of elements will be done in two steps. First, they will be mounted as well as possible in order to respect the optical acceptance of systems (each CCD must look at its mask or its LEDs). Second, their exact position relative to their associated chamber plane will be measured. It has been shown in this Section that specific requirements are not necessary. Position and orientation of all optical elements can easily be measured with precisions better than 1 mm and 1 mrad.

8.3   Effects of the optical system resolution

The GMS efficiency will depend on optical system resolutions, which will be affected by thermal fluctuations, inducing air disturbances [10, 11, 14], especially near the electronics of the chambers. Real dependence of PROX and BCAM resolutions on thermal effects are being tested in laboratory. We study in this Section how these losses of resolution affect the LMS efficiency.

PROX and BCAM are similar devices. If they were working with the same distance between their boxes, they would be affected in the same way. However, the working distance of BCAMs is much larger than the PROX one. Even if we don't know quantitatively how the fluctuations affect the resolution, we know that longer is the light path in the fluctuating medium, larger is the deterioration of the resolution. Consequently, BCAMs are much more affected than PROXs in the same thermal conditions. Nevertheless, we apply in this note the same factor of resolution loss for both PROXs and BCAMs. We thus largely overestimate the effects of thermal fluctuations on the PROX relative to the effects of these same fluctuations on the BCAM. The mounting accuracy of each optical element was fixed to 0.5 mm in position and 0.5 mrad in orientation.

Results are shown in Fig. 16. The value given in abscissa is the factor used to get the optical resolutions of both BCAMs and PROXs, multiplying their nominal values (Section 3). If we compare these results with the ones obtained in the previous Section (Fig. 15), one can observe that, despite a same resolution on relative positioning of TCs 8-9 monitored by BCAMs and a much better resolution for those monitored by PROXs, sagitta and mass resolutions are largely worse. Mispositioning and optical resolution effects having different behaviours when increasing the system size, this apparent mismatching is only due to the TCs we are looking at. Effectively, it was observed in the previous Section that the mispositioning effects on BCAMs measurements do not change a lot when increasing the distance separating the two boxes. Moreover, these effects increase with the range of displacements. Since the TCs 8 and 9 are larger than the other ones, the optical elements set on them are more displaced when the TCs rotate. As a consequence, in case of mispositioning, BCAM measurements are worse between TCs 8-9 than between the other ones. On the contrary, effects of optical resolution on BCAM measurements are directly proportional to the distance separating the two boxes, and independent on the range of displacements. Starting from Eq. (8), one can effectively
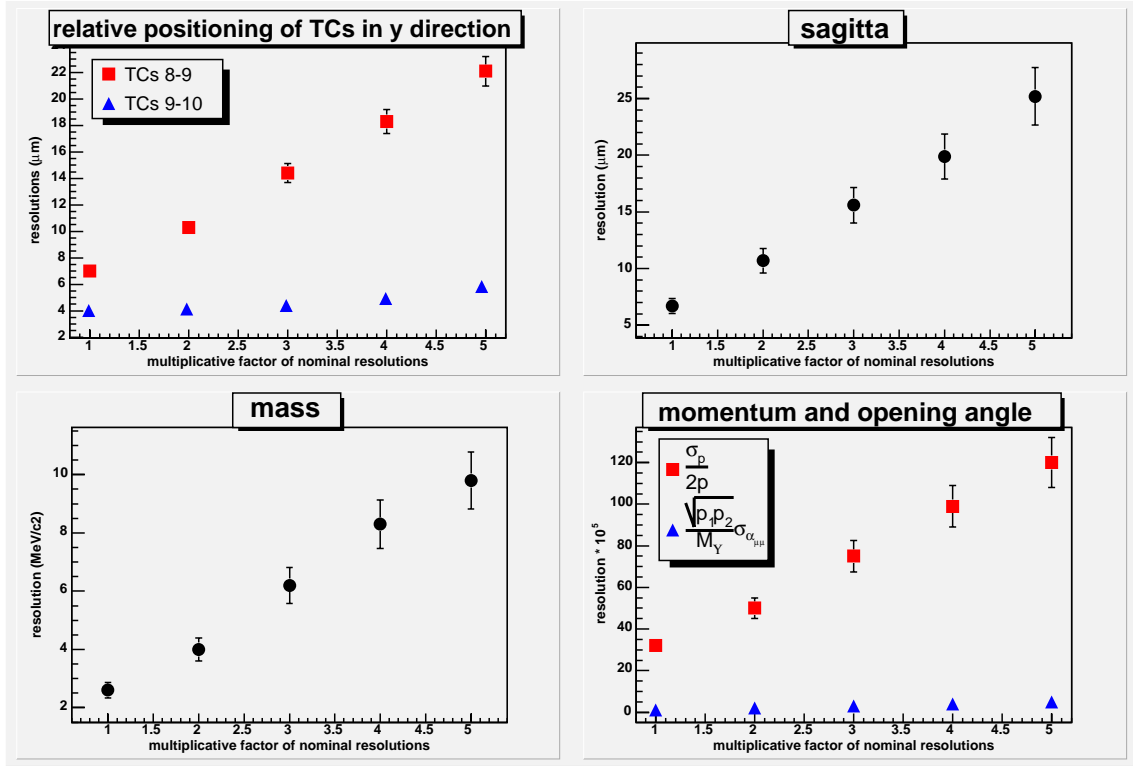
Figure 16: Effects of optical resolution on several quantities: **top left:** relative positioning accuracies between TCs 8-9 (monitored by BCAMs) and 9-10 (monitored by PROXs) in bending direction, using straight tracks uniformly distributed in the spectrometer acceptance; **top right:** fake sagitta induced on these straight tracks; **bottom left:** Υ mass resolution; **bottom right:** relative momentum ($\frac{\sigma_p}{2 \cdot p}$) and opening angle ($\frac{\sqrt{p_1 \cdot p_2}}{M_\Upsilon} \cdot \sigma_{\alpha_{\mu\mu}}$), using AliRoot. Nominal resolutions are the values presented in Section 3 (description of optical elements).

calculate:

$$\sigma_{dep_{LED}} = \frac{D_{LED-lens}}{d_{CCD-lens}} \cdot \sigma_{CCD_{mes}} \qquad (11)$$

In case of bad optical resolution, BCAM measurements are largely better between TC 8 and TC 9 than between TC 4 and TC 5 or between TC 6 and TC 7. To sumarize, the resolution on relative positioning between TC 4 and TC 5 and between TC 6 and TC 7 is largely worse in the case of bad optical resolution than in the case of optical element mispositioning, when the resolution on relative positioning between TC 8 and TC 9 is the same. This explains the different results obtained on sagitta and mass resolutions in this Section and in the previous one.

It clearly appears in the top left picture of Fig. 16 that BCAMs measurements of the TCs relative displacements are much more sensitive to the loss of optical resolution than the PROX ones are. The explanation is that, for BCAMs, the effect of this loss of resolution is multiplied by the distance separating the two boxes (see Eq. (11)). We can also observe on the same picture that the monitoring resolution of TC 9-10 does not depend linearly on the deteriorating factor. It means that even with a bad optical resolution,

the PROX inefficiency is dominated by geometrical uncertainties on the position of the chambers (from the calibration run) and of the optical elements.

In order to separate effects from BCAMs and from PROXs, sagitta and mass resolutions were calculated with 5 times the nominal resolution, first on BCAMs measurements, then on PROXs measurements. We obtained $\sigma_S = 24.4$ μm and $\sigma_M = 9.5$ MeV/c^2 for BCAMs, and $\sigma_S = 9.4$ μm and $\sigma_M = 4$ MeV/c^2 for PROXs. These results clearly show that the thermal effects will decrease the LMS efficiency principally through the deterioration of the BCAM resolution. This conclusion is even stronger if we recall that these effects on PROXs are overestimated in the simulation. First test in laboratory has shown that thermal effects on the BCAM measurements can be reduced by using air blowing. A loss of resolution reduced to a factor 3 was obtained. In such conditions, the LMS efficiency remains by far within requirements.

9   TCs 5-10 in two half planes: new LMS efficiency

The two half planes which compose the chambers 5 to 10 are mounted separately. As a result, independent rotations and translations may occur between the two half planes of a same chamber. The Longitudinal Monitoring System is able to measure these new displacement parameters (12 parameters instead of 6 for chambers 5 to 10). However, the number of degrees of freedom in the monitoring procedure (number of optical measurements - number of adjusted parameters) strongly decreases, reducing the LMS efficiency. We then found a sagitta resolution $\sigma_s = 23$ μm and a mass resolution $\sigma_M = 9$ MeV/c^2. The external monitoring was still supposed to be perfect. It means that the 6 displacement parameters of TC9 which correspond to the movement of its two half planes together were perfectly known. The 6 other parameters which correspond to the relative displacements of these two half planes were measured by the LMS. TCs 1 to 4 and the two half planes of TCs 5 to 10 were supposed to be rigid planes. The optical system installation accuracies were fixed to 0.5 mm and 0.5 mrad. The resolutions of optical devices were fixed to three times their nominal values (Section 3) to take into account the thermal effects.
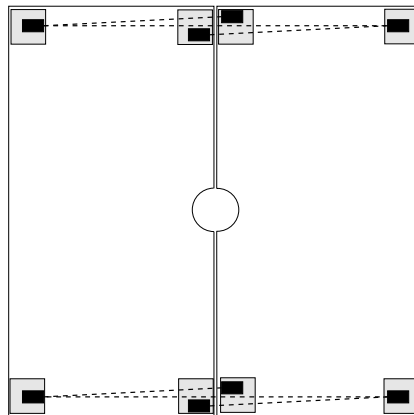

Figure 17: Schematic view of the transverse BCAM lines added to complete the LMS for stations 3, 4 and 5.

In order to improve these resolutions, 6 lines linking the 2 half planes of a same chamber were added to the previous LMS setup for TCs 5 to 10 (see Fig. 17). The BCAM boxes which are used on the central platforms are named "double" BCAM. On both faces, they have two laser diodes and one CCD which allows them to "look" and "shine" in both directions. The second optical line starting from these boxes (not shown in Fig. 17) is used to monitor the half chamber deformations (see Section 10). Thanks to these new measurements, sagitta resolution $\sigma_s = 17$ μm and mass resolution $\sigma_M = 7$ MeV/c^2 were achieved in the same simulation conditions. These values are closed to the ones obtained in the previous Section with the same resolutions of optical devices.
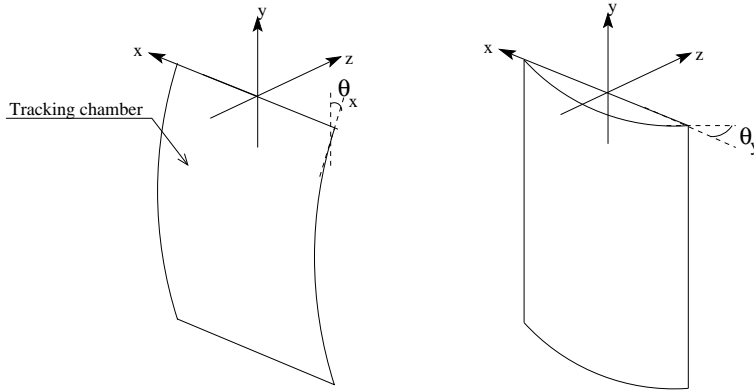
10 Chamber plane deformations: the TMS

Figure 18: Schematic view of the two easiest deformations that a support plane can experience.

All simulations performed above supposed that the tracking chambers (or the half tracking chambers) were rigid modules. Nevertheless, deformations are expected to occur during the long time of data taking. Their direct effects on the Υ mass resolution are expected to be low, since they are equivalent to displacements perpendiculary to the bending (vertical) direction of tracks. However, their indirect effects, through the decrease of the LMS efficiency, are very large as we can see in Section 10.1. The Transverse Monitoring System (TMS), measuring these deformations, is presented in Section 10.2. Its performances and their implications on the LMS efficiency are evaluated in Section 10.3. Finally, the loss of optical system resolution on both TMS and LMS is studied in Section 10.4. For all these simulations, the external monitoring is still supposed to be perfect.

10.1 Effects of chamber plane deformation on the LMS

As the optical elements which compose the LMS are installed on platforms at the corners of the (half) chamber supports, only the deformations which rotate or displace a corner relative to the others will have an effect on the LMS. A schematic view of the two easiest deformations a support plane can experience is shown in Fig. 18. Therefore, we simulated the deformation of the (half) chambers by allowing platform displacements and rotations.

The results shown in Fig. 19 were obtained by randomly rotating all the platforms around the two in-plane axis. In order to give an order of magnitude, an 1 mrad rotation angle corresponds, for a half chamber support of the station 5, to an 1.5 mm sagitta only over the 6 meters of its height.
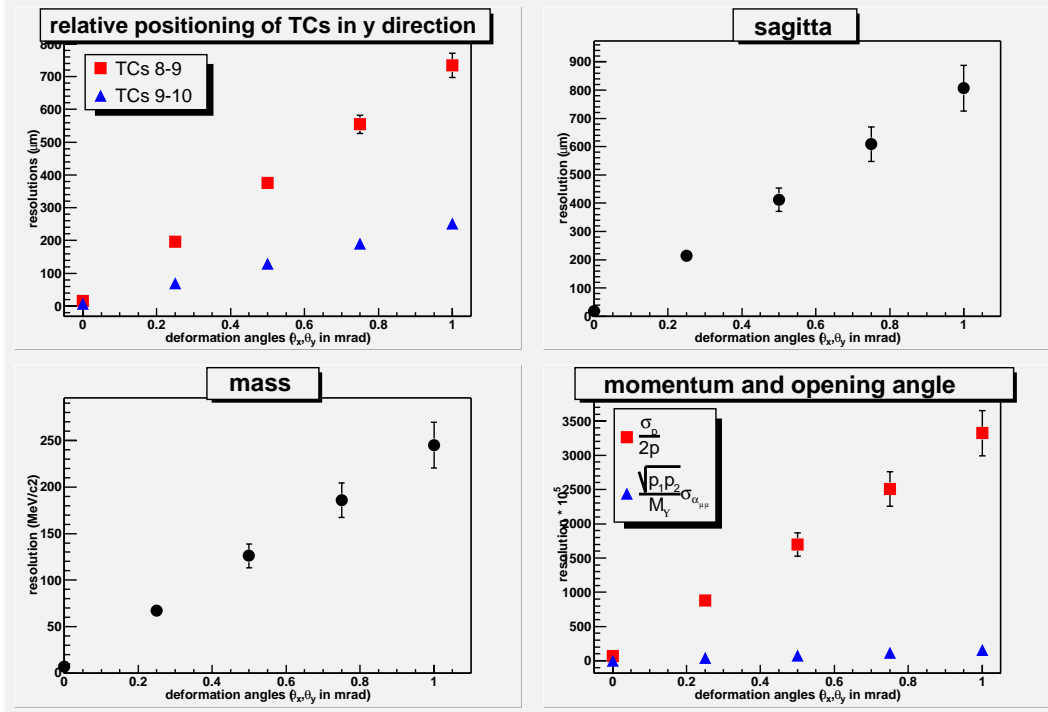

Figure 19: Effects of plane deformation on several quantities: **top left:** relative positioning accuracies between TCs 8-9 (monitored by BCAMs) and 9-10 (monitored by PROXs) in bending direction, using straight tracks uniformly distributed in the spectrometer acceptance; **top right:** fake sagitta induced on these straight tracks; **bottom left:** Υ mass resolution; **bottom right:** relative momentum ($\frac{\sigma_p}{2 \cdot p}$) and opening angle ($\frac{\sqrt{p_1 \cdot p_2}}{M_\Upsilon} \cdot \sigma_{\alpha_{\mu\mu}}$) using AliRoot.

The unexpected displacement, induced by platform rotations, and recorded by the optical elements, are interpreted by the Longitudinal Monitoring System as global chamber displacements. We can immediately see in Fig. 19 that it makes the LMS rapidly inefficient. It is clear that a system which monitors the flatness of the chambers and in particular the movement of platforms is needed.

10.2 The TMS setup

Due to the two different configurations used for the tracking stations, we developed two slightly different setups for the transverse monitoring system. The figure 20 shows a schematic view of the setup used to monitor the flatness of the chamber planes of stations 1 and 2. The figure 21 shows a schematic view of the setup used to monitor the flatness of the half chamber planes of stations 3, 4 and 5. In both cases, the array of BCAMs (black rectangles) allows to determine precisely the relative rotations and translations of

the four platforms which support the optical elements of the LMS. Bi-directional sources are used to complete the monitoring of the chamber shape.
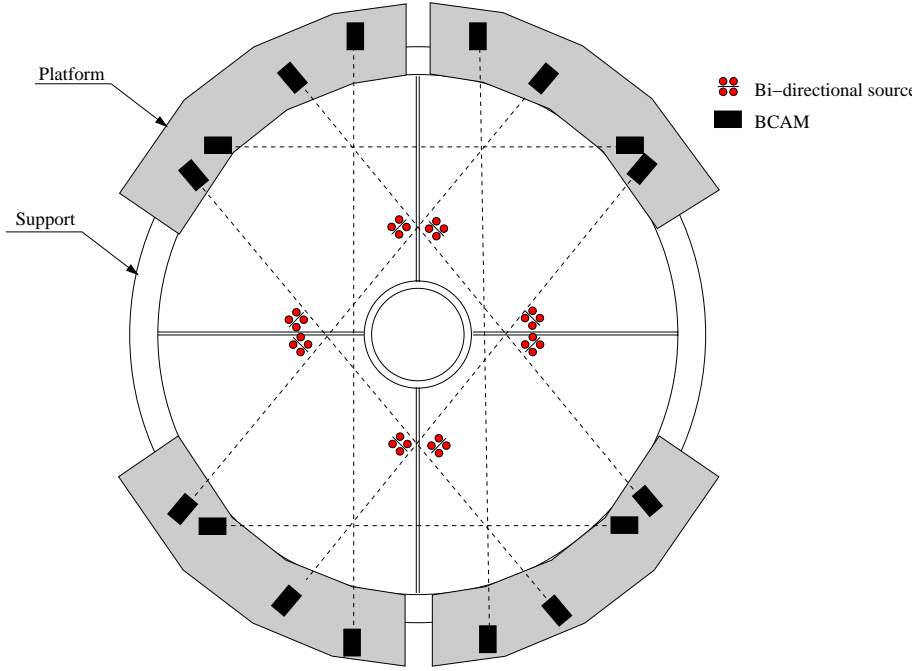

Figure 20: Schematic view of the transverse monitoring system of stations 1 and 2.
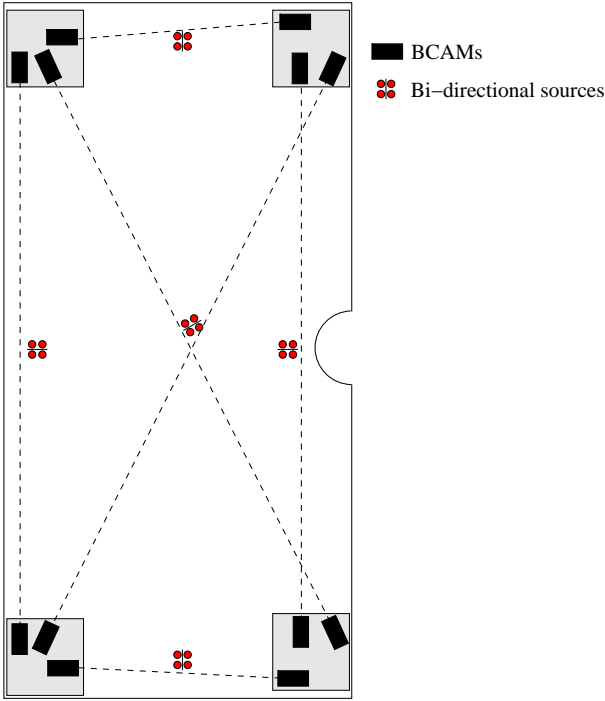

Figure 21: Schematic view of the transverse monitoring system of stations 3, 4 and 5.

10.3 The TMS performances, effects on the LMS efficiency

The Transverse Monitoring System (TMS) works like the LMS. Since the optical measurements give only access to relative movements, platforms and bi-directional sources on a same (half) chamber are monitored relative to one of the four platforms (which is fixed). Displacements of this particular platform are in fact directly correlated to displacements of the (half) chamber in its globality, like global displacements of the TC9 - which is the reference for the LMS - are directly correlated to global displacements of the entire spectrometer.

A (half) chamber plane can experience very complicated deformations which will change the orientation and the position of the platforms and of the bi-directional sources. Nevertheless, the most significant deformations are expected to be torsions around one or more in-plane axes. The simplest ones are depicted in Fig. 18. Displacements expected with such a kind of deformations are rotations around x and y axes and translations along the beam axis (z) for the platforms, and only translations along the beam axis for the bi-directional sources. In the simulations, the possible deformations are randomly generated using a 2-dimensional polynomium of degree 5. From this polynomium, we can extract the movements of platforms and bi-directional sources which are directly monitored by the TMS.

Station	σ_{θ_x} (μrad)	σ_{θ_y} (μrad)	σ_z (μm)
1	8.4	8.3	8.5
2	8.0	8.1	10.2
3	7.9	8.3	17.3
4	8.4	8.0	28.1
5	8.2	8.6	31.2

Table 4: Performances of the transverse monitoring system.

The table 4 gives the sigma of the residuals between the induced and the retrieved movements of the platforms. The optical system installation accuracies were fixed to 0.5 mm and 0.5 mrad, and the resolutions of the optical devices were kept at their nominal values (Section 3). We can see that the TMS will be able to monitor the rotation angles of the platforms at the level of 8 μrad. One can notice that the resolution achieved on the rotation angles is constant as a function of the station number. At the opposite, it is not the case for the resolution on the displacement along the z axis. σ_z increases with the station number due to the fact that the distance between the platforms get bigger as we go from station 1 to station 5, while the angular resolution of the BCAM is constant. By taking into account the platform displacements measured by the TMS, we can again perform the Longitudinal Monitoring with a good efficiency. We evaluated the new LMS performances using the same installation accuracies and optical resolutions as for the TMS. We obtained a sagitta resolution of 16 μm and a mass resolution of 6 MeV/c^2, which is by far within requirements. These values have to be compared to $\sigma_s = 7$ μm and $\sigma_M = 3$ MeV/c^2 which were obtained in the same simulation conditions with (half) chambers made of rigid modules.

Using the measured displacements of platforms and bi-directional sources, we are also able to reconstruct the global deformations of the (half) chambers. These deformations are reproduced with a 2-dimensionnal polynomium of degree 4 which is the best we can do with the available measurements. This polynomium is adjusted, using the MINUIT fitter, in order to reproduce as well as possible the displacement measurements. Translations correspond to a local value of the polynomium. Rotations correspond to a local value of its derivative. The TMS performances, in term of reconstruction of the global deformations, are evaluated *via* the re-positioning accuracies of one hundred points across the (half) chamber. We obtained an accuracy better than 100 μm for a half chamber from station 5 (the largest one). Simulations have shown that an uncertainty of 100 μm (along the beam axis) on all the interaction points of muons with the chambers induces an uncertainty of 4 μm on the sagitta and 2 MeV/c^2 on the mass. These values correspond to the direct effect of the TMS inefficiency. As expected, they are negligible as compared to the resolutions presented above and induced indirectly *via* the loss of LMS efficiency. Consequently, the direct effect of the TMS inefficiency will always be neglected in the next Sections.

10.4   Effect of the BCAM/PROX resolution on the TMS/LMS

It is clear, since movements of platforms are measured by only BCAMs, that thermal effects (through the optical resolution) will largely affect the TMS efficiency and, indirectly, the LMS performance. The optical element installation accuracies were still set to 0.5 mm and 0.5 mrad in the simulations.
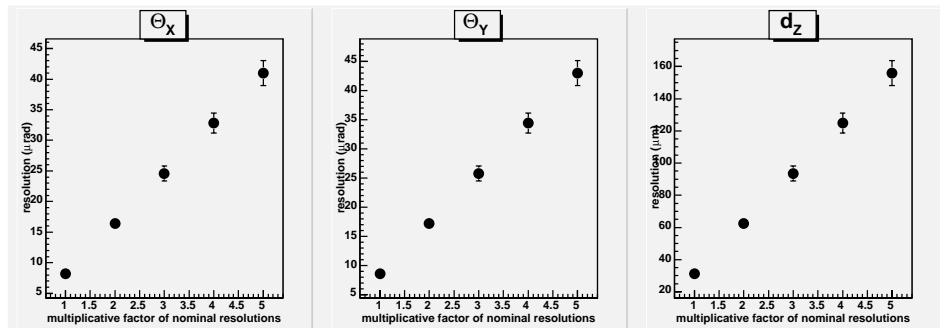

Figure 22: Effects of optical resolution on TMS efficiency of station 5: measurement accuracy of platform rotation around the no-bending direction (Θ_X); around the bending direction (Θ_Y); measurement accuracy of platform translation perpendicularly to the chamber plane (d_Z). Nominal resolutions are the values presented in Section 3 (description of optical elements).

Effects of loss of optical resolution on the TMS efficiency are shown in Fig. 22. Their influencies on the LMS performances are shown in Fig. 23. The values in abscissa are the factors being used to get the resolutions of both BCAMs and PROXs, by multiplying their nominal values (Section 3). In Fig. 23, this factor is applied on the optical systems of both the TMS and the LMS. All these results show the necessity to fight against the thermal effects. First tests in laboratory showed that if nothing is done, these effects can
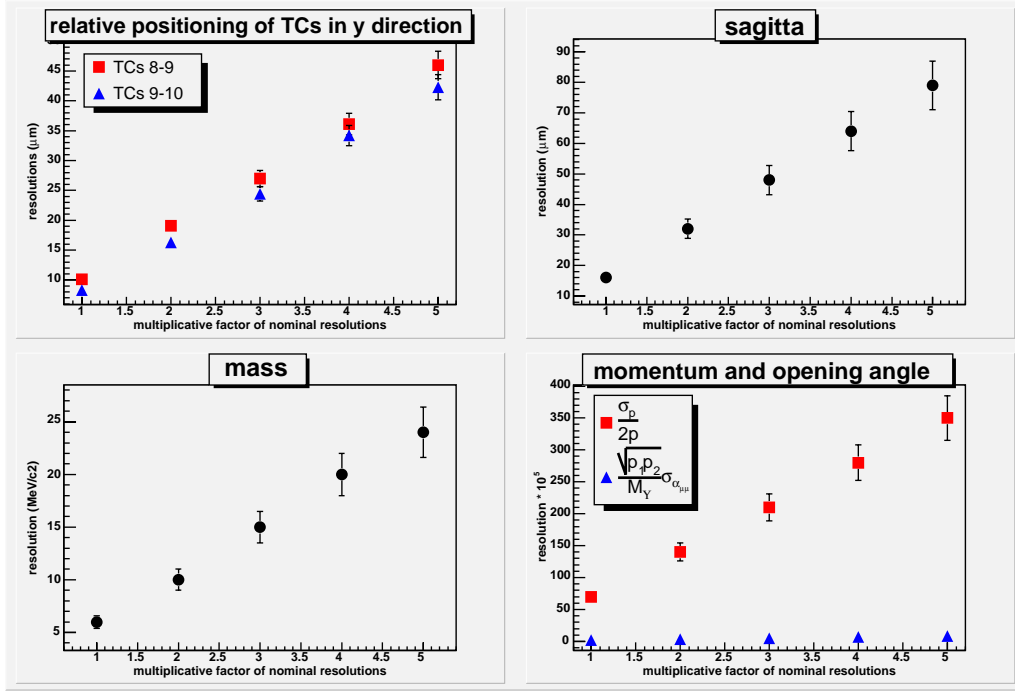
Figure 23: Effects of optical resolution on several quantities: **top left:** relative positioning accuracies between TCs 8-9 (monitored by BCAMs) and 9-10 (monitored by PROXs) in bending direction, using straight tracks uniformly distributed in the spectrometer acceptance; **top right:** fake sagitta induced on these straight tracks; **bottom left:** Υ mass resolution; **bottom right:** relative momentum ($\frac{\sigma_p}{2 \cdot p}$) and opening angle ($\frac{\sqrt{p_1 \cdot p_2}}{M_\Upsilon} \cdot \sigma_{\alpha_{\mu\mu}}$), using AliRoot. Nominal resolutions are the values presented in Section 3 (description of optical elements).

induce a deterioration of BCAM resolution by a factor greater than 5. Nevertheless, as it was already mentioned in Section 8.3, the same tests showed that this factor can be reduced to 3 by using air blowing. This solution allows to reach a LMS efficiency within requirements.

11 Effects of devices's breakdowns

We tested the robustness of the system against breakdowns of optical devices by shutting down artificially one or more optical lines inside the system and we extracted induced displacements and deformations using the resulting incomplete system. In this Section, the mounting accuracies of each optical element were fixed to 0.5 mm in position and 0.5 mrad in orientation. The resolutions of both BCAM and PROX devices were fixed to three times their nominal values (Section 3) to take into account effects of thermal fluctuations. The TMS is also performed in addition to the LMS to monitor the platform displacements. In the Sections 11.1 and 11.2, the external monitoring is still supposed to be perfect. The robustness of the EMS against breakdowns is evaluated in Section 11.3 only.

11.1 Breakdowns in the LMS

We need eight optical lines to monitor a chamber from station 1 or 2 relative to another chamber, and fourteen to monitor a chamber from station 3 to 5 (8 lines between the monitored chamber and the reference chamber, and 6 lines between the 2 half planes of the monitored chamber). The effects of devices's breakdowns on the performances of the LMS were simulated by removing randomly a certain number of optical lines inside these groups of 8 or 14 lines. In the case of BCAM, removing one line means removing the four images given by the four laser diodes. The figure 24 shows the results of these simulations. The value given in abscissa is the number of lines broken down among each of these groups of 8 or 14 lines. As expected, the resolution on the mass and the sagitta deteriorates with the number of breakdowns. One can see that when only 1 of 8 or 14 lines (BCAMs or PROXs) breaks, the resolution loss is negligible. With 4 breakdowns in each group of lines, the resolution loss is fairly big with in addition 6% of total loss of efficiency when MINUIT does not properly converge. More precise study showed that such convergence problems occur when all the optical lines linking a half chamber to a next chamber break down.
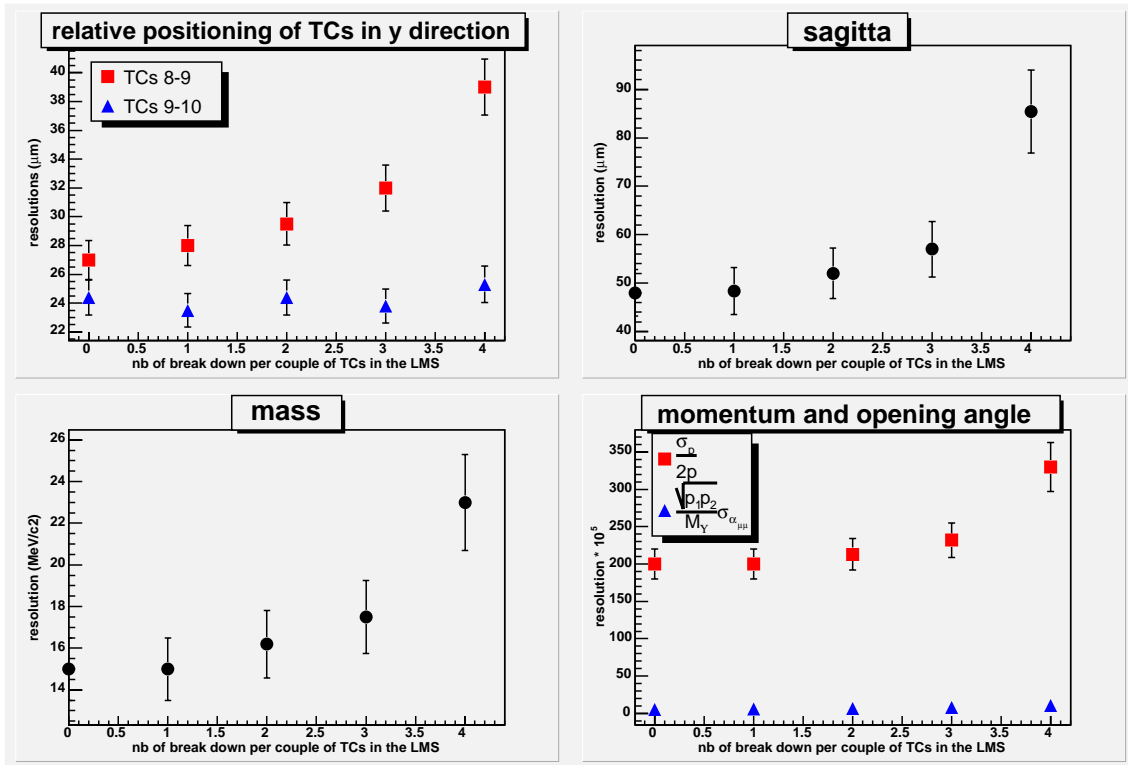

Figure 24: Effects of breakdowns on several quantities: **top left:** relative positioning accuracies between TCs 8-9 (monitored by BCAMs) and 9-10 (monitored by PROXs) in bending direction, using straight tracks uniformly distributed in the spectrometer acceptance; **top right:** fake sagitta induced on these straight tracks; **bottom left:** Υ mass resolution; **bottom right:** relative momentum ($\frac{\sigma_p}{2 \cdot p}$) and opening angle ($\frac{\sqrt{p_1 \cdot p_2}}{M_\Upsilon} \cdot \sigma_{\alpha_{\mu\mu}}$), using AliRoot.

We can conclude that the LMS is robust up to at least 3 breakdowns among the 8 or 14 lines used to monitor a chamber relative to another. In this case, MINUIT always properly converges. One has to recall that these simulations of breakdowns were carried out by removing a given number of lines inside EACH group of 8 or 14 lines. In the case where only one group is affected, the LMS remains fully efficient. Effectively, if we randomly remove 3 lines inside one group randomly chosen, we obtain the same results as without any breakdown.

11.2   Breakdowns in the TMS

As for the LMS, the effects of devices's breakdowns on the performances of the TMS were simulated by removing randomly a given number of optical lines on a (half) chamber. The figure 25 shows the results of this simulation on the accuracies of platform displacements. The value given in abscissa is the number of lines broken down on each (half) chamber. We can observe looking at the angular resolutions or the MINUIT inefficiencies that the TMS is more robust against breakdowns on stations 1 and 2. This is due to the fact that 8 BCAM lines are used in the setup for chambers 1 to 2 (Fig. 20) while only 6 BCAMs equip each half chambers 5 to 10 (Fig. 21) to monitor the same number of platforms. Nevertheless, we can see that for all (half) chambers, the system is fully working (no lost due to minimization errors) if only one breakdown occurs and may not properly work in the case of two breakdowns. The resolutions given in this last case was obtained by excluding the events where MINUIT did not converge properly.

number of breakdowns per chamber	$\sigma_{sagitta}$ (μm)	σ_M (MeV/c^2)
0	48	15
1	68	21
2	112	35

Table 5: Resolution on the sagitta and the Υ mass as a function of the number of device's breakdowns per chamber.

It was shown in the previous Section that the LMS efficiency is very sensitive to the measurement accuracies of platform displacements. Consequently, breakdowns on the TMS affect the saggita and mass resolution, as we can see in Table 5. In these simulations the quoted number of lines broken down was randomly removed on all the (half) chambers. We can observe that in the case of one breakdown per (half) chamber, the resolutions are still good enough. In the case of two breakdowns, and in spite of excluding the events where MINUIT did not converge properly, the resolutions exceed requirements. Simulations were also carried out with 1 breakdown on only one (half) chamber randomly chosen. In that case, the sagitta and mass resolutions are similar to the situation without breakdowns.
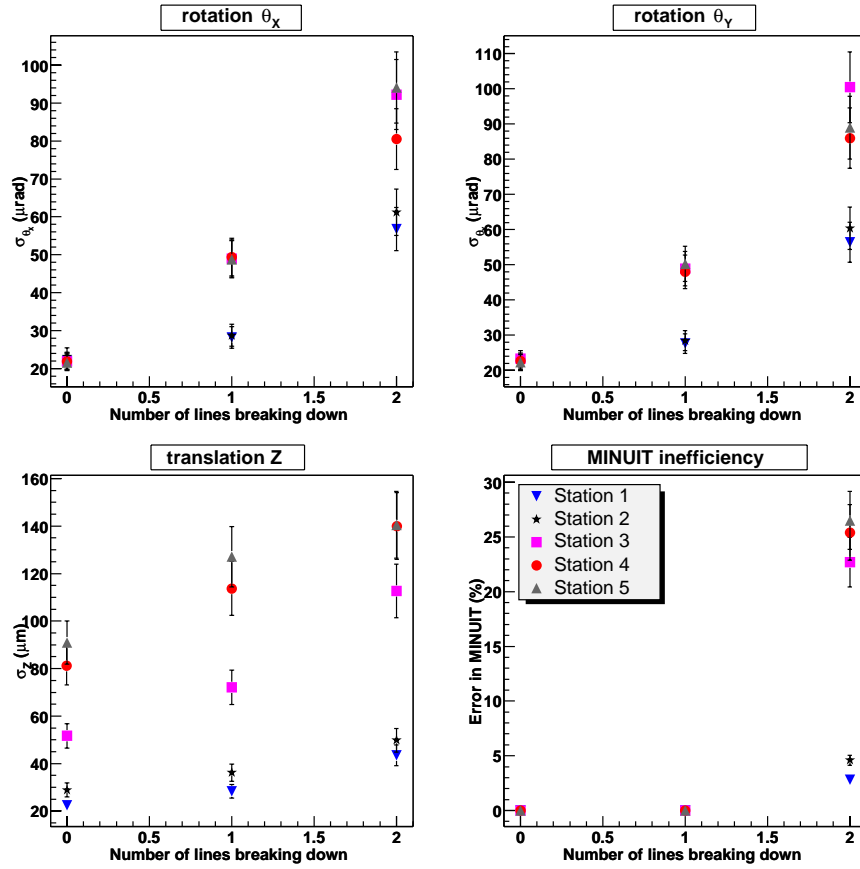
Figure 25: Effects of breakdowns on several quantities: resolutions on the measurements of platform rotations (θ_X, θ_Y) and translations (Z), percent of minimization errors.

11.3 Breakdowns in the EMS

In order to reduce the CPU time consuming, we supposed in the previous studies that the external monitoring was perfectly performed. Of course this is not the case but we assumed that the Υ mass resolution did not depend by a significant way on the EMS efficiency. Before studying effects of breakdowns in the EMS, we checked whether this assumption was correct. The wall deformations are taken into account by applying random local displacements in the ranges ± 1 mm and ± 1 mrad.

number of breakdowns per chamber	σ_M (MeV/c^2)	$\sigma_{p_{T_\Upsilon}}$ (MeV/c)	σ_{y_Υ} ($\times 10^{-4}$)	minimization efficiency (%)
0	15	56	21	100
1	15	58	22	100
2	16	78	28	95

Table 6: Resolution on the Υ mass, transverse momentum p_{T_Υ} and rapidity y_Υ, percent minimization efficiency, as a function of the number of device's breakdowns per chamber.

The first line in Table 6 shows the results of the simulation of the GMS in its globality (without breakdown). If we compare the mass resolution with the one quoted in the first line in Table 5 obtained by assuming a perfect external monitoring, we can immediately conclude that, as expected, the EMS inefficiency has no significant effect. We can also compare the results on p_{T_Υ} and y_Υ resolutions with the ones obtained in Section 7, where the optical resolutions of BCAMs and PROXs were fixed to their nominal values and each chamber was supposed to be one rigid module. We can see that the rapidity resolution which only depends on the EMS efficiency is about the same. It means that the performances of the EMS are here only limited by the unexpected wall deformations. If the walls were fixed, these performances would be better and also more affected by the loss of resolution of the optical devices and by the chamber deformations. The p_{T_Υ} resolution is different because it depends both on the global orientation of the spectrometer (measured by the EMS) and on the absolute momentum resolution (depending on the LMS efficiency).

The effect of breakdowns in the EMS are presented in the two last lines in Table 6. We can see that one optical line broken down at each side of the spectrometer does not change significantly the results. The EMS is robust. If two lines break down among the 4 lines linking the spectrometer to the wall on each side, the p_{T_Υ} and y_Υ resolutions decrease and MINUIT may not converge properly.

12 Summary

The Geometry Monitoring System (GMS) of the muon spectrometer was defined and its performances evaluated by simulation. It is composed of three parts: the Longitudinal (LMS), the External (EMS) and the Transverse (TMS) Monitoring Systems.

In this note, we showed that the LMS as described in Section 4 allows to measure accurately the relative displacement of chambers (when they are supposed to be rigid modules), providing us with sagitta and Υ mass resolutions well under requirements. It was also shown, that about the same monitoring accuracies are reachable by adding 6 optical lines to monitor the additional relative displacement of the two half planes of chambers 5-10 (stations 3-5). Since the choice of the external links (EMS) to monitor the TC9 has no effect on these resolutions, the simplest setup was selected. We also showed that accuracies on optical element positions and orientations better than 1 mm and 1 mrad are sufficient to reach a good monitoring efficiency. Such accuracies are easily reachable. We can also note that the optical element mispositioning is the main source of inaccuracy for PROXs. Unexpected chamber deformations make the LMS totally inefficient if platforms on which the optical devices are mounted are not monitored with a high accuracy. Simulations showed that the TMS is efficient enough to provide us with sagitta and Υ mass resolutions still within requirements. Thermal effects on the GMS performances, through the deterioration of resolutions of optical elements, were also studied. It was shown that only the BCAM measurements are affected. It was also shown that the loss of resolution must be lower than a factor 4 relative to the nominal one in order to stay under requirements. Extrapolating laboratory tests, we expect this factor to be of the order of 3 in the spectrometer working conditions. In such conditions,

simulations showed that the resolutions achievable by the complete GMS are 48 μm for the sagitta and 15 MeV/c^2 for the Υ mass. Studies in the latest Section finally showed that this system is robust against breakdowns.

Acknowledgments

References

[1] ALICE Collaboration, CERN/LHCC 99-22, (1999), Technical Design Report of the Dimuon Forward Spectrometer.

[2] ALICE Collaboration, CERN/LHCC 2000-046, (2000), Addendum to the Technical Design Report of the Dimuon Forward Spectrometer.

[3] R. Tieulent *et al.*, Internal Note/DIM, ALICE-INT-2005-009, The Geometry Monitoring System of the ALICE Dimuon Spectrometer, Overview, April, 28, 2005.

[4] P. Pillot, Thesis, Université Claude Bernard, Lyon I, 2005.

[5] http://morsch.home.cern.ch/morsch/MUONdoc/

[6] http://AliSoft.cern.ch/offline/

[7] S. GRIGORYAN *et al.*, Internal Note/DIM, ALICE-INT-2003-051, Using Muons to Align Tracking Chambers in the ALICE Dimuon Forward Spectrometer, November 14, 2003.

[8] A. SCHRICKER, The Alignment System of the ATLAS Muon End-Cap Spectrometer, August 13, 2002.

[9] H. GULKANYAN, Apparent Sagitta Measurement with RASNIK. Internal Report of YerPhI/ALICE group, September 1999.

[10] G. DICKER, NIKHEF, Linearity, Resolution, and Systematic Errors of the CCD - RASNIK Alignment System, May - July, 1997.

[11] K. S. HASHEMI *et al.*, ATLAS Internal Note, The BCAM Camera, September 15, 2000.

[12] F. JAMES AND M. ROOS, Comp. Phys. Comm. **10** (1975) 343; http://consult.cern.ch/writeup/minuit

[13] W. COOSEMANS *et al.*, The alignment of the LHC low beta triplets: review of intrumentation and methods.

[14] A. SCHRICKER, ATLAS Muon Note, Refractive Bending of Light due to Thermal Gradients in Air, October 24, 2001.
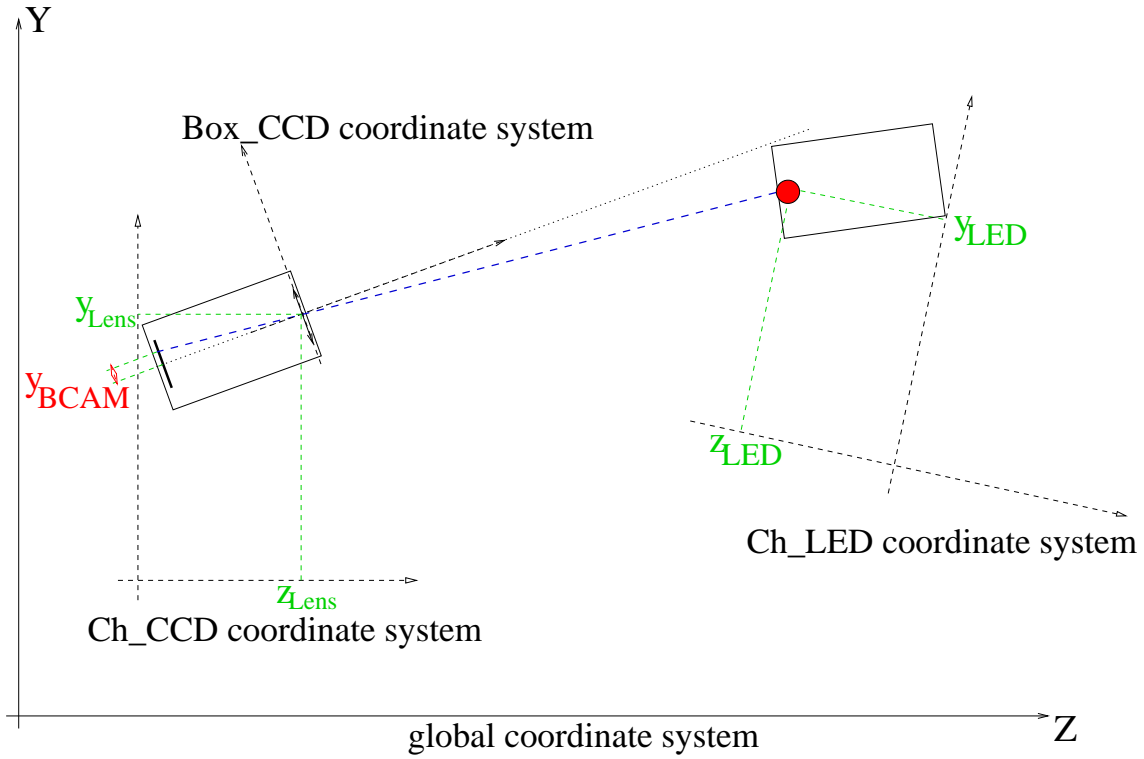
A Calculation of BCAM measurements

Figure 26: BCAM measurements.

The BCAM system measures the position of the two LEDs images on the CCD. In order to simulate these measurements, one has to use the position of the two boxes on their chambers and the position of the two chambers in the global coordinate system of the spectrometer (see Fig. 26).

- $\text{Box}_{CCD \ or \ LED}$ = box supporting CCD and lens, or box supporting LEDs

- $\text{Ch}_{CCD \ or \ LED}$ = chamber supporting $\text{Box}_{CCD \ or \ LED}$

- $\begin{pmatrix} x_{lens \ or \ LED} \\ y_{lens \ or \ LED} \\ z_{lens \ or \ LED} \end{pmatrix}$ = lens or LED position in the $\text{Ch}_{CCD \ or \ LED}$ coordinate system

- $\begin{pmatrix} x_{Ch_{CCD \ or \ LED}} \\ y_{Ch_{CCD \ or \ LED}} \\ z_{Ch_{CCD \ or \ LED}} \end{pmatrix}$ = $\text{Ch}_{CCD \ or \ LED}$ position in the global coordinate system

- $\begin{pmatrix} x \\ y \\ z \end{pmatrix}$ = LED position in the Box_{CCD} coordinate system

36

To pass from global to chamber coordinate system one uses passive rotations:

$$\mathcal{R}_{Glob \to Ch} = \mathcal{R}_X \mathcal{R}_Y \mathcal{R}_Z \tag{12}$$

with:

$$\mathcal{R}_X = \begin{pmatrix} 1 & 0 & 0 \\ 0 & \cos\theta_X & \sin\theta_X \\ 0 & -\sin\theta_X & \cos\theta_X \end{pmatrix}, \mathcal{R}_Y = \begin{pmatrix} \cos\theta_Y & 0 & -\sin\theta_Y \\ 0 & 1 & 0 \\ \sin\theta_Y & 0 & \cos\theta_Y \end{pmatrix}, \mathcal{R}_Z = \begin{pmatrix} \cos\theta_Z & \sin\theta_Z & 0 \\ -\sin\theta_Z & \cos\theta_Z & 0 \\ 0 & 0 & 1 \end{pmatrix}$$

Same kind of matrices are used to pass from chamber to box coordinate system (note that z axis of the Box_{CCD} coordinate system link the CCD center with the lens center and that x and y axes are oriented like CCD):

$$\mathcal{R}_{Ch \to Box} = \mathcal{R}_x \mathcal{R}_y \mathcal{R}_z \tag{13}$$

Of course, the reverse transformations can be achieved using the transposed matrices.

With these known values, one can calculate the LED position in the Box_{CCD} coordinate system by applying successively the change of coordinate system $(Ch_{LED} \to Glob \to Ch_{CCD} \to Box_{CCD})$:

$$\begin{pmatrix} x_1 \\ y_1 \\ z_1 \end{pmatrix} = {}^t(\mathcal{R}_{Glob \to Ch_{LED}}) \cdot \begin{pmatrix} x_{LED} \\ y_{LED} \\ z_{LED} \end{pmatrix} + \begin{pmatrix} x_{Ch_{LED}} \\ y_{Ch_{LED}} \\ z_{Ch_{LED}} \end{pmatrix} - \begin{pmatrix} x_{Ch_{CCD}} \\ y_{Ch_{CCD}} \\ z_{Ch_{CCD}} \end{pmatrix} \tag{14}$$

$$\begin{pmatrix} x \\ y \\ z \end{pmatrix} = \mathcal{R}_{Ch_{CCD} \to Box_{CCD}} \cdot \left[\mathcal{R}_{Glob \to Ch_{CCD}} \cdot \begin{pmatrix} x_1 \\ y_1 \\ z_1 \end{pmatrix} - \begin{pmatrix} x_{Lens} \\ y_{Lens} \\ z_{Lens} \end{pmatrix} \right] \tag{15}$$

Knowing the characteristics of a BCAM box, one can calculate the BCAM measurements:

- $D_{CCD-lens}$ = distance between CCD and lens

- x_{BCAM} = position x of the LED on CCD

- y_{BCAM} = position y of the LED on CCD

$$x_{BCAM} = \frac{D_{CCD-lens}}{z} \times x \tag{16}$$

$$y_{BCAM} = \frac{D_{CCD-lens}}{z} \times y \tag{17}$$

If (half) chambers and/or platforms holding BCAM elements are displaced, then equations (14) and (15) become more complicated. One has to introduce new changes of coordinate system in order to take into account the new parameters. Nevertheless, the principle is the same and the last two equations do not change.
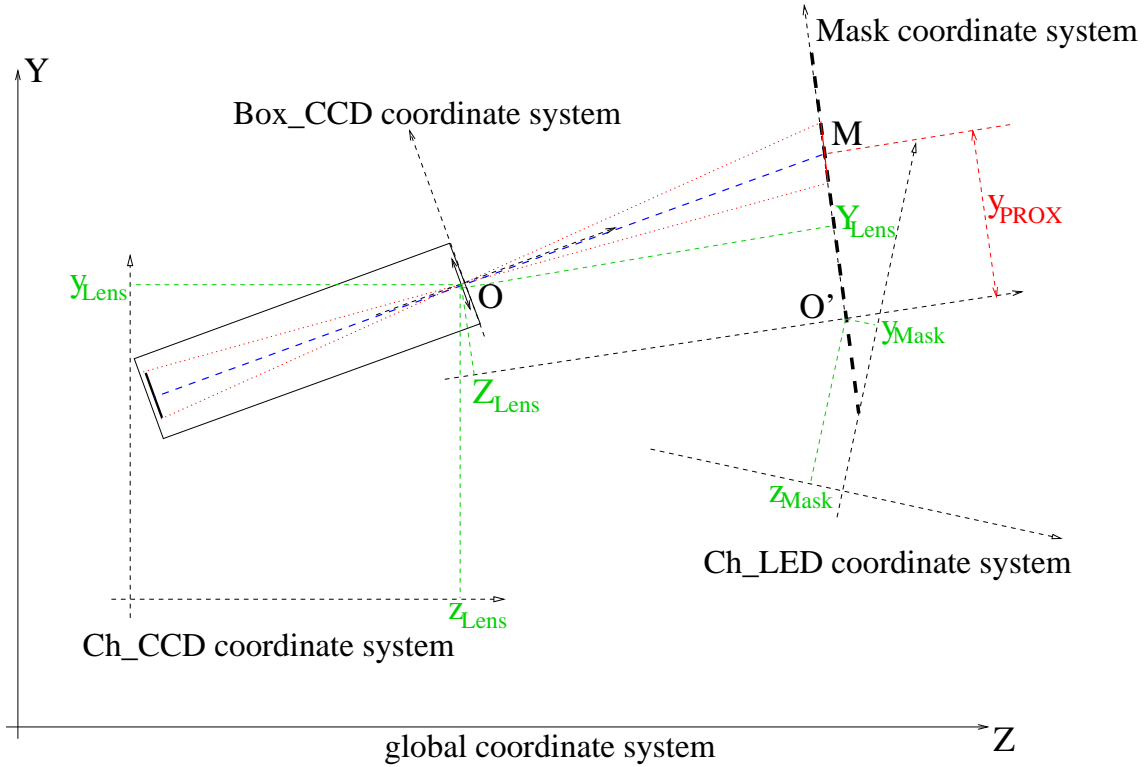
B Calculation of PROX measurements

Figure 27: PROX measurements.

The PROX system measures which part of the mask is filmed by the CCD and gives its characteristics (position on the mask, size and orientation relative to the CCD). As for BCAM measurements (Annexe A), one has to use the position of both CCD box and mask on their chambers and the position of the two chambers in the global coordinate system of the spectrometer in order to simulate PROX measurements (see Fig. 27).

- Box_{CCD} or mask = box supporting CCD and lens, or mask

- $Ch_{CCD \ or \ mask}$ = chamber supporting Box_{CCD} or mask

- $\begin{pmatrix} x_{lens \ or \ mask} \\ y_{lens \ or \ mask} \\ z_{mens \ or \ mask} \end{pmatrix}$ = lens or mask position in the $Ch_{CCD \ or \ mask}$ coordinate system

- $\begin{pmatrix} x_{Ch_{CCD \ or \ mask}} \\ y_{Ch_{CCD \ or \ mask}} \\ z_{Ch_{CCD \ or \ mask}} \end{pmatrix}$ = $Ch_{CCD \ or \ mask}$ position in the global coordinate system

To pass from global to chamber coordinate system one uses passive rotations:

$$\mathcal{R}_{Glob \to Ch} = \mathcal{R}_X \mathcal{R}_Y \mathcal{R}_Z \tag{18}$$

with:

$$\mathcal{R}_X = \begin{pmatrix} 1 & 0 & 0 \\ 0 & \cos\theta_X & \sin\theta_X \\ 0 & -\sin\theta_X & \cos\theta_X \end{pmatrix}, \mathcal{R}_Y = \begin{pmatrix} \cos\theta_Y & 0 & -\sin\theta_Y \\ 0 & 1 & 0 \\ \sin\theta_Y & 0 & \cos\theta_Y \end{pmatrix}, \mathcal{R}_Z = \begin{pmatrix} \cos\theta_Z & \sin\theta_Z & 0 \\ -\sin\theta_Z & \cos\theta_Z & 0 \\ 0 & 0 & 1 \end{pmatrix}$$

Same kind of matrices are used to pass from chamber to CCD box or mask coordinate system (note that the Box_{CCD} coordinate system is oriented as the BCAM one):

$$\mathcal{R}_{Ch\to Box} = \mathcal{R}_x \mathcal{R}_y \mathcal{R}_z \tag{19}$$

Of course, the reverse transformations can be achieved using the transposed matrices.

To find the characteristics of the filmed part of the mask, one have to calculate the image of the CCD center, on the mask (i.e. the intersection point of the line joining center of CCD and center of lens with the mask). With the notations of Fig. 27, one can write:

$$\overrightarrow{O'M} = \overrightarrow{O'O} + \overrightarrow{OM} \tag{20}$$

with (in the mask coordinate system):

$$\overrightarrow{O'M} = \begin{pmatrix} x_{PROX} \\ y_{PROX} \\ 0 \end{pmatrix}, \quad \overrightarrow{O'O} = \begin{pmatrix} X_{Lens} \\ Y_{Lens} \\ Z_{Lens} \end{pmatrix}, \quad \overrightarrow{OM} = \begin{pmatrix} a \cdot D \\ b \cdot D \\ c \cdot D \end{pmatrix}$$

where a, b and c are the cosinus director of the line, and D is the distance lens-intersection point.

So, we have to calculate the vector director of the line and the position of the lens, in the mask coordinate system:

vector director of the line in the Box_{CCD} coordinate system $= \begin{pmatrix} 0 \\ 0 \\ 1 \end{pmatrix}$

$$\begin{pmatrix} a \\ b \\ c \end{pmatrix} = \mathcal{R}_{Ch_{mask}\to mask} \cdot \mathcal{R}_{Glob\to Ch_{mask}} \cdot$$

$$ {}^t\mathcal{R}_{Glob\to Ch_{Box_{CCD}}} \cdot {}^t\mathcal{R}_{Ch_{Box_{CCD}}\to Box_{CCD}} \cdot \begin{pmatrix} 0 \\ 0 \\ 1 \end{pmatrix} \tag{21}$$

$$\begin{pmatrix} x_1 \\ y_1 \\ z_1 \end{pmatrix} = {}^t\mathcal{R}_{Glob\to Ch_{Box_{CCD}}} \cdot \begin{pmatrix} x_{lens} \\ y_{lens} \\ z_{lens} \end{pmatrix} + \begin{pmatrix} x_{Ch_{CCD}} \\ y_{Ch_{CCD}} \\ z_{Ch_{CCD}} \end{pmatrix} - \begin{pmatrix} x_{Ch_{mask}} \\ y_{Ch_{mask}} \\ z_{Ch_{mask}} \end{pmatrix} \tag{22}$$

$$\begin{pmatrix} X_{lens} \\ Y_{lens} \\ Z_{lens} \end{pmatrix} = \mathcal{R}_{Ch_{mask}\to mask} \cdot \left[\mathcal{R}_{Glob\to Ch_{mask}} \cdot \begin{pmatrix} x_1 \\ y_1 \\ z_1 \end{pmatrix} - \begin{pmatrix} x_{mask} \\ y_{mask} \\ z_{mask} \end{pmatrix} \right] \tag{23}$$

To calculate the relative orientation between mask and CCD, we have to calculate the image of an other point of the CCD, on the mask. The simpliest solution is to take a point

39

on the y axis of the CCD (at the top edge for example). Only the vector director of the line will change, so we have just to replace $\begin{pmatrix} 0 \\ 0 \\ 1 \end{pmatrix}$ by $\begin{pmatrix} 0 \\ \frac{t_{CCD}}{\sqrt{t_{CCD}^2 + D_{CCD-lens}^2}} \\ \frac{t_{CCD}}{\sqrt{t_{CCD}^2 + D_{CCD-lens}^2}} \end{pmatrix}$ in Eq. (21) (meaning of t_{CCD} and $D_{CCD-lens}$ are given below). The image position of this point can then be calculated exactly in the same way that the image position of the CCD center.

Knowing the characteristics of a PROX box and using equations (20), (21) and (23), one can calculate the characteristics of the filmed part of the mask:

- $D_{CCD-lens}$ = distance between CCD and lens

- t_{CCD} = size of the CCD

- x'_{PROX} = image position x of a point of the y axis of the CCD

- y'_{PROX} = image position y of a point of the y axis of the CCD

- x_{PROX} = position x of the filmed part of the mask

- y_{PROX} = position y of the filmed part of the mask

- M_{PROX} = Magnification

- s_{PROX} = size of the filmed image

- α_{PROX} = orientation of the mask relative to the CCD

$$x_{PROX} = -\frac{Z_{Lens} \times a}{c} + X_{Lens} \tag{24}$$

$$y_{PROX} = -\frac{Z_{Lens} \times b}{c} + Y_{Lens} \tag{25}$$

$$M_{PROX} = -\frac{c \times D_{CCD-lens}}{Z_{Lens}} \tag{26}$$

$$s_{PROX} = \frac{t_{CCD}}{M_{PROX}} \tag{27}$$

$$\alpha_{PROX} = \arctan\left(\frac{x'_{PROX} - x_{PROX}}{y'_{PROX} - y_{PROX}}\right) \tag{28}$$

If (half) chambers and/or platforms holding PROX elements are displaced, then equations (21), (22) and (23) become more complicated. One has to introduce new changes of coordinate system in order to take into account the new parameters. Nevertheless, the principle is the same and the last five equations do not change.